Benchmark for three-dimensional explicit asynchronous absorbing layers for ground wave propagation and wave barriers

Sijia Li, Michael Brun, Sergey Kuznetsov, Irini Djeran-Maigre

Benchmark for three-dimensional explicit asynchronous absorbing layers for ground wave propagation and wave barriers

Sijia Li[a], Michael Brun[a], Irini Djeran-Maigre[a], Sergey Kuznetsov[b]

[a] *Univ Lyon, INSA-Lyon, GeoMaS, 69621Villeurbanne, France*

[b] *Institute for Problems in Mechanics, 119526 Moscow, Russia*

Abstract

This paper presents a benchmark for three-dimensional explicit asynchronous absorbing layers for modeling unbounded domains through a standard displacement-based finite element method: Three-dimensional Perfectly Matched Layers (PML) is compared to recently proposed Absorbing Layers with Increasing Damping (ALID) based on Rayleigh and Kosloff damping formulations.

The coupled problem, including the interior subdomain and the absorbing layers, is implemented in the framework of Heterogeneous Asynchronous Time Integrator (HATI), enabling the absorbing layers to be handed with an explicit Central Difference scheme, with fine time steps, independently from the time stepping procedure adopted in the interior subdomain. Simple 3D Lamb's tests are considered by using different kinds of absorbing layers. The superiority of the PML in terms of the accuracy and computation time is highlighted. Finally, realistic 3D applications are investigated, such as the Lamb's test and the study of the screening effect provided by a horizontal wave barrier in mitigating the ground surface vibration generated by an excited plate.

Keywords: Perfectly Matched Layers (PML), Absorbing Layers with Increasing Damping, Rayleigh Damping, Kosloff Damping, Subdomain Coupling, Heterogeneous Asynchronous Time Integrator

1. Introduction

The isolation of buildings against shocks and propagating waves in the soil becomes a more and more important problem due to the increasing intensity of machine foundations and human activities such as railway and highway traffic. Indeed, modern equipments such as computers and accurate measurement instruments, may be affected by the induced vibrations. Moreover, people who live near these disturbance sources become more sensitive to the industrial vibrations and cannot increase their tolerance for the inconvenience and discomfort [1]. Thus, there is a strong need to reduce the vibration experienced by people, structures and equipments by using isolation systems. Wave barriers corresponding to various obstacles such as open trenches and solid barriers composed of different materials [2], constitute examples of isolation measures that can be used against soil vibrations. The design of wave barriers motivated the development of analytical and numerical tools for analyzing their isolating effect on traveling waves [3, 4], using the Boundary Element Method (BEM) in the frequency domain. In most cases, the problem characterized by the complex geometry, boundary conditions and nonlinear material behavior laws for the soil, has to be dealt by using the Finite Element Method (FEM), advocating the FEM/BEM coupling approach in three-dimensional analysis, in the frequency domain [5] or in the time domain [6]. Wave propagation in unbounded domains is very efficiently predicted by the BEM approach, which provides exact radiation conditions; however, the method is preferably dedicated to weak heterogeneities and linear constitutive models [7]. When adopting the FEM

approach, or other spatial discretization methods such as Finite Difference (FD) or Spectral Element Method (SEM), accurate boundary conditions have to be applied to the boundaries of the truncated domain. As a result, several kinds of artificial boundaries have been developed to avoid spurious waves, such as the infinite elements (Bettess [8], Houmat [9]), absorbing boundary conditions (Enquist et al. [10] , Liu and Zhao [11]), absorbing layer methods (Kosloff and Kosloff [12], Semblat et al. [13], Rajagopal et al. [14] , Zafati et al.[15], Li et al. [16]) and PML (Perfect Matched Layers).

The PML was proposed by Bérenger [17] for absorbing electromagnetic waves and was interpreted shortly after by Chew 1994[18] in terms of complex coordinate stretching. The PML is endowed with the remarkable features that the same attenuation is provided for all the frequencies and is reflectionless in a continuous setting for all angles of incidence at the interface, making it more efficient than the other absorbing layers. The first PML adapted to the elastodynamic equations was formulated according to a split procedure for the components of velocities with respect to the interface (Chew and Liu [19], Collino and Tsoga [20]). Then, the unsplit-formulation, called C–PML, was developed by Wang et al. [21] in the context of the finite difference method, requiring the computation of convolution integrals, which was later extended by Matzen [22] to the finite element method. Basu and Chopra [23, 24] proposed a displacement-based unsplit formulation for two-dimensional time-domain elastodynamics and extended it to the three-dimensional case in explicit dynamics [25], which was implemented in the Finite Element software LS-DYNA and DIANA [26,27]. Convolution integrals were avoided but additional quantities were required such as integrals in time of strains and stresses. The issue of computing integrals in time of strains and stresses was circumvented by Kucukcoban and Kallivokas [28] by introducing a combined stress-displacement formulation, at the expense of the increase of the system size to be solved. The authors also gave an extensive survey of the various

PML formulations. To avoid increasing the computation cost in the interior domain, hybrid formulation was proposed, using a primal coupling approach (Kucukcoban and Kallivokas [29]), which was finally extended to three-dimensional problems by Fathi et al. [30]. Brun et al. [31] implemented Basu and Chopra's formulation for two-dimensional problems, using a dual coupling approach with Lagrange multipliers. It was realized in the framework of Heterogeneous (different time integrators) Asynchronous (different time steps) Time Integrator [32,33], so as to integrate the PML with an implicit time integrator using an appropriate time step size, irrespective of the time integration parameters for the interior domain.

Here, three-dimensional complex wave propagation problems are focused, such as the mitigation of ground surface vibration through Horizontal Wave Barrier (HWB), set up close to an excited plate, representing, for instance, the slab track excited by the tramway wheels [34]. For this purpose, a full explicit three-dimensional PML with an efficient method for calculating the internal force is developed using the HATI framework. It enables us to adopt the Central Difference (CD) method with a fine time step in the PML in order to enhance the accuracy of the PML, while keeping the classical finite element formulation without complex-valued stretched coordinates in the interior domain.

Using the proposed HATI framework, other absorbing layers, which are more convenient to be implemented in FE software, are also investigated and compared with the PML: Absorbing Layers with Increasing Damping (ALID) using viscous Rayleigh damping (Zafati et al. [15], Li et al. [35]) and ALID with Kosloff damping (Li et al. [16]). In the case of Rayleigh damping, it is widely known that introducing Rayleigh damping reduces the critical time step [35,36]. As a consequence, fine time steps can be independently employed in the ALID based on Rayleigh damping thanks to the proposed HATI framework, while the interior domain is integrated using a Newmark explicit time integration scheme with a time step satisfying the CFL condition, which

is not affected by the introduction of Rayleigh damping. In the cases of PML and Kosloff ALID, although the critical time step in explicit dynamics is unchanged, fine time steps in the absorbing layers are also investigated for accuracy improvement.

In this paper, we first present the strong form in the time domain of three-dimensional PML, followed by the weak form of the coupled problem, including the non-dissipative interior subdomain and PML subdomain. The coupling is ensured thanks to the introduction of the Lagrange multipliers so as to satisfy the velocity continuity at the interface. Then, finite element and space discretization is carried out, by focusing on explicit time integration with Central Difference (CD) method, in order to reduce the computation time in the three-dimensional PML. By taking advantage of the versatility of the HATI framework, ALID based on Rayleigh and Kosloff damping are also presented for 3D dynamic problems. In numerical applications, a first simple 3D Lamb's problem, including only one hexahedral element in the thickness, is investigated; results obtained from PML are compared with results obtained from Rayleigh and Kosloff ALID, demonstrating the superiority of the PML in terms of the accuracy and computation time. A 3D Lamb's test with same dimensions in the two horizontal directions is then simulated with the proposed PML as well as a more complex case, including two plates lied on the ground, where the first one corresponds to the excited plate and the second one corresponds to the Horizontal Wave Barrier (HWB). Influence of the design parameters, such as the length, width and depth of the HWB, is assessed in terms of the reduction of ground displacement.

2. Perfectly Matched Layer

The 3D-PML is inspired from Basu's formulation [25], by developing an efficient method for calculating the internal force and extending it to multi-time step computation. We focus on multi-

time step explicit integration for the purpose of efficient computation in unbounded domains. The goal is to treat in a complete independent way the absorbing layers, with respect to the interior domain with the time step corresponding to the CFL condition. The formulation of the proposed explicit multi time step 3D-PML is given in this section and will be compared to previously published Absorbing Layers with Increasing Damping (ALID) based on different damping formulations, that are Rayleigh and Kosloff damping, whose main advantage with respect to the PML is their simplicity for the implementation in a finite element code.

2.1 Strong form of the three-dimensional PML

The PML is formulated by introducing the complex-valued stretching functions into the classical elastodynamic equations in the frequency domain. First, we introduce the complex-valued stretching function $\lambda_i(x_i)$, enabling to replace the real coordinate x_i with the complex coordinate ones $\tilde{x}_i$:

$$\frac{\partial \tilde{x}_i}{\partial x_i} = \lambda_i(x_i) = 1 + f_i^e(x_i) + \frac{f_i^p(x_i)}{i\omega} \tag{1}$$

where ω denotes the circular frequency, the attenuation function f_i^p which is positive real-valued as a function of x_i, serves to attenuate the propagating waves in the x_i direction, whereas the scaling function f_i^e attenuates the evanescent waves by stretching the coordinate variable x_i. It has to be noted that this expression is the same as that chosen by Kucukcoban and Kallivokas [29] and Fathi et al [30]. It is slightly different from the one adopted by Basu and Chopra [23, 24] and Basu [25], in order to avoid introducing a characteristic length of the problem under consideration. The complex coordinate is then employed in the equation of motion in the frequency domain, giving the following governing equations for wave propagation in PML domain:

$$\sum_j \frac{1}{\lambda_j(x_j)} \frac{\partial \sigma_{ij}}{\partial x_j} = -\omega^2 \rho u_i \tag{2}$$

$$\sigma_{ij} = \sum_{k,l} C_{ijkl} \varepsilon_{kl} \tag{3}$$

$$\varepsilon_{ij} = \frac{1}{2}\left[\frac{1}{\lambda_j(x_j)} \frac{\partial u_i}{\partial x_j} + \frac{1}{\lambda_i(x_i)} \frac{\partial u_j}{\partial x_i}\right] \tag{4}$$

where σ_{ij}, ε_{ij} are the components of the stress and strain tensors; C_{ijkl} are the components of the elastic constitutive tensor for homogeneous isotropic medium and the last equation gives the deformation relationship under small deformation assumption. The following notations are introduced for the PML domain: Ω_{PML}, bounded by the $\Gamma_{PML} = \Gamma_{PML}^D + \Gamma_{PML}^N$, where $\Gamma_{PML}^D \cap \Gamma_{PML}^N = \emptyset$, defining the decomposition of the boundary conditions into Dirichlet and Neumann conditions.

Thanks to the introduction of the stretching functions expressed in Eq. (1), the inverse Fourier transform can be easily applied to the previous frequency-domain equations, leading to the following equations in time domain:

$$div\left(\underline{\underline{\sigma}}\,\underline{\underline{\tilde{F}}}^{ee} + \underline{\underline{\Sigma}}\,\underline{\underline{\tilde{F}}}^{ep} + \underline{\underline{\tilde{\Sigma}}}\,\underline{\underline{\tilde{F}}}^{pp}\right) = \rho f_M \underline{\ddot{u}} + \rho f_C \underline{\dot{u}} + \rho f_K \underline{u} + \rho f_H \underline{U} \tag{5}$$

$$\underline{\underline{\sigma}} = \underline{\underline{C}} : \underline{\underline{\varepsilon}} \tag{6}$$

$$\underline{\underline{F}}^{eT}\,\underline{\underline{\dot{\varepsilon}}}\,\underline{\underline{F}}^{e} + \left(\underline{\underline{F}}^{pT}\,\underline{\underline{\varepsilon}}\,\underline{\underline{F}}^{e} + \underline{\underline{F}}^{eT}\,\underline{\underline{\varepsilon}}\,\underline{\underline{F}}^{p}\right) + \underline{\underline{F}}^{pT}\,\underline{\underline{E}}\,\underline{\underline{F}}^{p}$$

$$= \frac{1}{2}\left[\underline{\underline{F}}^{eT}\left(\nabla \underline{\dot{u}}\right) + \left(\nabla \underline{\dot{u}}\right)^T \underline{\underline{F}}^{e}\right] + \frac{1}{2}\left[\underline{\underline{F}}^{pT}\left(\nabla \underline{u}\right) + \left(\nabla \underline{u}\right)^T \underline{\underline{F}}^{p}\right] \tag{7}$$

where the PML matrices $\underline{\underline{\tilde{F}}}^{ee}$, $\underline{\underline{\tilde{F}}}^{ep}$, $\underline{\underline{\tilde{F}}}^{pp}$, $\underline{\underline{F}}^{e}$, $\underline{\underline{F}}^{p}$, as well as the scalar-valued functions f_M, f_C, f_K and f_H depend on the scaling function $f_i^e(x_i)$ and the attenuation function $f_i^p(x_i)$. Their expressions are given in Appendix A. Due to the use of the inverse Fourier transform, the 3D

PML time domain formulation requires successive time integrals of stress and strain tensors, which are defined by: $\underline{\underline{\Sigma}} = \int_0^t \underline{\underline{\sigma}}\, \mathrm{d}t$, $\underline{\underline{\tilde{\Sigma}}} = \int_0^t \underline{\underline{\Sigma}}\, \mathrm{d}t$ and $\underline{\underline{E}} = \int_0^t \underline{\underline{\varepsilon}}\, \mathrm{d}t$; in addition, the time integral of displacement has to be computed, given by $\underline{U} = \int_0^t \underline{u}\, \mathrm{d}t$. The previous equations are complemented with Dirichlet and zero traction forces at the Neumann conditions:

$$\begin{cases} \underline{u} = 0 & on\ \Gamma_{PML}^{D} \\ \left(\underline{\underline{\sigma}}\,\underline{\underline{\tilde{F}}}^{ee} + \underline{\underline{\Sigma}}\,\underline{\underline{\tilde{F}}}^{ep} + \underline{\underline{\tilde{\Sigma}}}\,\underline{\underline{\tilde{F}}}^{pp}\right)\underline{n} = 0 & on\ \Gamma_{PML}^{N} \end{cases} \tag{8}$$

It has to be remarked that the equation of motion in Eq. (5) is a third-order differential equation, with four fields: the displacement field, velocity field, acceleration field and time integral of the displacement field. In Basu's formulation [25] the same equation of motion was obtained with one multiplicative factor that comes from the definition of a slightly different complex-valued stretching function as noted previously. Eq. (6) is the classical constitutive relationship and Eq. (7), identical to Basu's formulation, describes a much more complex deformation relationship than that of the classic relationship, involving the strain, strain derivative in time and time integral of the strain. In the following, assumptions concerning the calculation of strain will be made in order to integrate in time the governing equations according to the explicit Central Difference scheme.

2.2 Weak form of the coupled problem

Let Ω be a bounded domain belonging to $\mathbb{R}^3$ with a regular boundary. J= [0, T] is the time interval of interest. The domain Ω is divided into two partitions Ω_1 and Ω_2, as shown in Fig.1, such as: $\Omega_1 \cap \Omega_2 = \emptyset$ and $\partial\Omega_1 \cap \partial\Omega_2 = \Gamma_I$. Γ_I denotes the interface between the two subdomains, subdomain Ω_1 represents the non-dissipative medium (the domain of interest) and subdomain Ω_2 represents the PML medium.

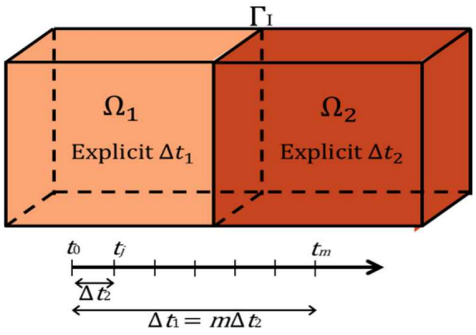

178

179 Fig. 1 Domain Ω divided into two subdomains Ω_1 (interior subdomain) and Ω_2 (PML subdomain)

180 The subdomain 1 is assumed to be isotropic linear elastic and the subdomain 2 is related to
181 the PML. The subdomain Ω_1 is characterized by its density ρ_1, Young's modulus E_1, Poisson's
182 coefficient ν_1, $\underline{b}_1$ the body force, $\underline{u}_1^D$ the Dirichlet prescribed displacement on Γ_1^D and $\underline{g}_1^N$ the
183 traction force at the Neumann condition on Γ_1^N. The subdomain Ω_2 is characterized by its
184 density ρ_2, Young's modulus E_2, Poisson's coefficient ν_2, $\underline{b}_2$ the body force, $\underline{u}_2^D$ the Dirichlet
185 prescribed displacement on Γ_2^D, and $\underline{g}_2^N$ the traction force at the Neumann condition on Γ_2^N.The
186 coupled problem in Ω divided into two partitions Ω_1 and Ω_2. The classic test functions $\underline{v}_1$ and $\underline{v}_2$,
187 belonging to the appropriate spaces, are introduced: $\underline{v}_1 \in W_1^* = \left\{\underline{v}_1 \in \left(H^1(\Omega_1)\right)^d and\ \underline{v}_1 =\right.$
188 $\left. 0\ on\ \Gamma_1^D\right\}$, $\underline{v}_2 \in W_2^* = \left\{\underline{v}_2 \in \left(H^1(\Omega_2)\right)^d and\ \underline{v}_2 = 0\ on\ \Gamma_2^D\right\}$, where d is the space dimension,
189 equal to 3. The solutions belong to the following spaces: $\underline{u}_1(t) \in W_1, W_1 = \left\{\underline{u}_1 \in\right.$
190 $\left.\left(H^1(\Omega_1)\right)^d and\ \underline{u}_1 = u_1^D on\ \Gamma_1^D\right\}, \underline{u}_2(t) \in W_2, W_2 = \left\{\underline{u}_2 \in \left(H^1(\Omega_2)\right)^d and\ \underline{u}_2 = u_2^D on\ \Gamma_2^D\right\}$.

191 According to a dual Schur approach, the introduction of the Lagrange multipliers allows us
192 to glue the velocities of the two subdomains at the interface Γ_I [37, 38]. The Lagrange multipliers
193 belong to the adapted dual trace space related to the interface between the two subdomains,
194 denoted by Q. All the considered space variables are assumed to be sufficiently smooth and

regular. Next, using a dual Schur formulation, the principle of virtual power for transient dynamics can be written. Find the solution $\underline{u}_1(t) \in W_1$, $\underline{u}_2(t) \in W_2$ and $\underline{\lambda}(t) \in Q$, for which the following weak form is satisfied $\forall \underline{v}_1 \in W_1^*$, $\forall \underline{v}_2 \in W_2^*$ and $\forall \underline{\mu} \in Q$:

$$\int_{\Omega_1} \rho_1 \underline{v}_1 \cdot \underline{\ddot{u}}_1 d\Omega + \int_{\Omega_1} \underline{\underline{\varepsilon}}(\underline{v}_1) : \underline{\underline{\sigma}}_1 d\Omega + \int_{\Omega_2} \rho f_M \underline{v}_2 \cdot \underline{\ddot{u}}_2 \mathrm{d}\Omega + \int_{\Omega_2} \rho f_C \underline{v}_2 \cdot \underline{\dot{u}}_2 \mathrm{d}\Omega + \int_{\Omega_2} \rho f_K \underline{v}_2 \cdot \underline{u}_2 \mathrm{d}\Omega$$

$$+ \int_{\Omega_2} \rho f_H \underline{v}_2 \cdot \underline{U}_2 \mathrm{d}\Omega + \int_{\Omega_2} \underline{\underline{\tilde{\varepsilon}}}^{ee} : \underline{\underline{\sigma}} \mathrm{d}\Omega + \int_{\Omega_2} \underline{\underline{\tilde{\varepsilon}}}^{ep} : \underline{\underline{\Sigma}} \mathrm{d}\Omega + \int_{\Omega_2} \underline{\underline{\tilde{\varepsilon}}}^{pp} : \underline{\underline{\tilde{\Sigma}}} \mathrm{d}\Omega$$

$$+ \int_{\Gamma_I} \underline{v}_1 \cdot \underline{\lambda} d\Gamma + \int_{\Gamma_I} \underline{v}_2 \cdot \underline{\lambda} d\Gamma + \int_{\Gamma_I} \underline{\mu} \cdot (\underline{\dot{u}}_1 - \underline{\dot{u}}_2) d\Gamma$$

$$= \int_{\Omega_1} \underline{v}_1 \cdot \underline{b}_1 d\Omega + \int_{\Gamma_1^N} \underline{v}_1 \cdot \underline{g}_1^N d\Gamma + \int_{\Gamma_2^N} \underline{v}_2 \cdot (\underline{\underline{\sigma}} \tilde{F}^{ee} + \underline{\underline{\Sigma}} \tilde{F}^{ep} + \underline{\underline{\tilde{\Sigma}}} \tilde{F}^{pp}) n \mathrm{d}\Gamma \qquad (9)$$

with the expression of the modified strain tensors in the PML subdomain, taking into account the scaling and damping functions:

$$\begin{cases} \underline{\underline{\tilde{\varepsilon}}}^{ee} = \frac{1}{2}\left[(\nabla \underline{v}) \underline{\underline{\tilde{F}}}^{ee} + \underline{\underline{\tilde{F}}}^{eeT} (\nabla \underline{v})^T \right] \\ \underline{\underline{\tilde{\varepsilon}}}^{ep} = \frac{1}{2}\left[(\nabla \underline{v}) \underline{\underline{\tilde{F}}}^{ep} + \underline{\underline{\tilde{F}}}^{epT} (\nabla \underline{v})^T \right] \\ \underline{\underline{\tilde{\varepsilon}}}^{pp} = \frac{1}{2}\left[(\nabla \underline{v}) \underline{\underline{\tilde{F}}}^{pp} + \underline{\underline{\tilde{F}}}^{ppT} (\nabla \underline{v})^T \right] \end{cases} \qquad (10)$$

Then, by using the above expressions, the internal force in the weak form in Eq. (9) can be written as:

$$p_{int}^e = \int_{\Omega} \underline{\underline{\tilde{\varepsilon}}}^{ee} : \underline{\underline{\sigma}} d\Omega + \int_{\Omega} \underline{\underline{\tilde{\varepsilon}}}^{ep} : \underline{\underline{\Sigma}} d\Omega + \int_{\Omega} \underline{\underline{\tilde{\varepsilon}}}^{pp} : \underline{\underline{\tilde{\Sigma}}} d\Omega \qquad (11)$$

In Eq. (9), the right hand side term related to the Neumann condition for the PML subdomain, that is $\int_{\Gamma_2^N} \underline{v}_2 \cdot (\underline{\underline{\sigma}} \tilde{F}^{ee} + \underline{\underline{\Sigma}} \tilde{F}^{ep} + \underline{\underline{\tilde{\Sigma}}} \tilde{F}^{pp}) n \mathrm{d}\Gamma$, becomes equal to zero due to Eq. (8).

2.3 Space and time discretization

Here, we focus on the coupling between two explicit time integrators, with two different time scales, the large time step $\Delta t_1 = [t_0; t_m]$ for the interior domain and the fine time step $\Delta t_2 = [t_{j-1}; t_j]$ for the absorbing layers. This choice is imposed by the fact that we want to keep explicit time integrators in both subdomains for the calculation efficiency in three-dimensional complex modelling and the use of different damping formulations in the absorbing layers. For instance, it is well known that the introduction of Rayleigh damping matrix reduces the critical time step size of the Central Difference scheme [36]. Second, in the PML case, it was shown in Brun et al. [31] and Li et al. [16] that PML accuracy of Basu's formulation is very sensitive to the time step size, advocating for a fine time step in the PML.

We follow the classical finite element discretization, by adopting 8-node hexahedral element with linear shape functions. The approximation of the displacement is given by: $u_e(x, y, z) = \mathbf{N}(x, y, z)\mathbf{U_e}$, where $\mathbf{U_e}$ gathers the nodal displacements of the 8 nodes, with a size of 24×1; the matrix $\mathbf{N}(x, y, z)$, with a size 3×24, contains the nodal shape functions: $\mathbf{N}(x, y, z) = [N_1\mathbf{I} \quad N_2\mathbf{I} \quad \cdots \quad N_8\mathbf{I}]$, where $\mathbf{I}$ is the 3×3 identity matrix. First, we discretize the interface power terms of the weak form in Eq. (9), related to the coupling between subdomains. At the interface between the subdomains, the continuity of velocities is imposed by the following condition:

$$\mathbf{L_1}\dot{\mathbf{U}}_\mathbf{1} + \mathbf{L_2}\dot{\mathbf{U}}_\mathbf{2} = 0 \tag{12}$$

where $\mathbf{L_1}$ and $\mathbf{L_2}$ are the Boolean constraint matrices in the case of matching meshes at the interface Γ_I. In the case of non-matching meshes, the mortar approach has to be applied, leading to non-Boolean constraint matrices $\mathbf{L_1}$ and $\mathbf{L_2}$[39]. They operate on nodal vectors associated with the two subdomains and pick out the degrees of freedom belonging to the interface Γ_I in order to

ensure the velocity continuity at the interface. The restricted velocity vectors on the interface are given by $\mathbf{L_1\dot{U}_1}$ and $\mathbf{L_2\dot{U}_2}$, whereas the operators $(\mathbf{L_1})^T$ and $(\mathbf{L_2})^T$ represent the prolongation operators from the interface to the subdomains. Using the Boolean constraint matrices, the interface terms in the weak form can be expressed as:

$$\begin{cases} \int_{\Gamma_I} \underline{v_1} \cdot \underline{\lambda} d\Gamma = \mathbf{V_1^T L_1^T \lambda} \\ \int_{\Gamma_I} \underline{v_2} \cdot \underline{\lambda} d\Gamma = \mathbf{V_2^T L_2^T \lambda} \end{cases} \tag{13}$$

From the weak form in Eq. (9), we write the equation of motion related to the interior subdomain Ω_I, at the time t_m, that is the end of the large time step $\Delta t_1 = [t_0; t_m]$:

$$\mathbf{M_1 \ddot{U}_1^m + K_1 U_1^m = F_1^{ext,m} - L_1^T \lambda^m} \tag{14}$$

Concerning the PML subdomain, we write the equation of motion at time t_j , at the end of the fine time step $\Delta t_2 = [t_{j-1}; t_j]$:

$$\mathbf{M_2 \ddot{U}_2^j + \left(C_2 + \tilde{C}_2\right)\dot{U}_2^{j-1/2} + \left(K_2 + \widetilde{K}_2\right)U_2^j + \overline{K}_2 \overline{U}_2^j + P_2\left(\varepsilon_{j-1}, E_{j-1}, \Sigma_{j-1}, \widetilde{\Sigma}_{j-1}\right)}$$

$$\mathbf{= F_2^{ext,j} - L_2^T \hat{\lambda}^j} \tag{15}$$

The derivation and expression of the matrices involved in Eq. (15) and the internal force are detailed in Appendix A. Briefly, the inertial system matrices $\mathbf{M_2}$, $\mathbf{C_2}$, $\mathbf{K_2}$ and $\overline{\mathbf{K}}_2$are assembled from their respective element-level matrices. The element-level matrices are obtained by adopting a quadrature formula in every hexahedral element:

$$\mathbf{M_2^e} = \int_{\Omega^e} \rho f_M \mathbf{N^T N} \, d\Omega \tag{16}$$

$$\mathbf{C_2^e} = \int_{\Omega^e} \rho f_C \mathbf{N^T N} \, d\Omega \tag{17}$$

$$\mathbf{K_2^e} = \int_{\Omega^e} \rho f_K \mathbf{N^T N}\, \mathrm{d}\Omega \tag{18}$$

$$\overline{\mathbf{K}}^{\mathbf{e}} = \int_{\Omega^e} \rho f_H \mathbf{N^T N}\, \mathrm{d}\Omega \tag{19}$$

In Eq. (15), the other PML matrices $\tilde{\mathbf{C}}_\mathbf{2}$ and $\widetilde{\mathbf{K}}_\mathbf{2}$ come from the space and time discretization of the internal force corresponding to the terms $\int_{\Omega_2} \underline{\underline{\tilde{\varepsilon}}}^{ee} : \underline{\underline{\sigma}} \mathrm{d}\Omega + \int_{\Omega_2} \underline{\underline{\tilde{\varepsilon}}}^{ep} : \underline{\underline{\Sigma}} \mathrm{d}\Omega + \int_{\Omega_2} \underline{\underline{\tilde{\varepsilon}}}^{pp} : \underline{\underline{\tilde{\Sigma}}} \mathrm{d}\Omega$ in the weak form in Eq. (9). $\tilde{\mathbf{C}}_\mathbf{2}$ and $\widetilde{\mathbf{K}}_\mathbf{2}$ are defined at the element-level by:

$$\tilde{\mathbf{C}}_\mathbf{2}^\mathbf{e} = \int_{\Omega_e} \widetilde{\mathbf{B}}^\mathbf{T} \frac{1}{\Delta t} \mathbf{D} \mathbf{B}^{\boldsymbol{\varepsilon}} d\Omega \tag{20}$$

$$\widetilde{\mathbf{K}}_\mathbf{2}^\mathbf{e} = \int_{\Omega_e} \widetilde{\mathbf{B}}^\mathbf{T} \frac{1}{\Delta t} \mathbf{D} \mathbf{B}^{\mathbf{Q}} d\Omega \tag{21}$$

where PML matrices $\widetilde{\mathbf{B}}^{\mathbf{ee}}$, $\widetilde{\mathbf{B}}^{\mathbf{ep}}$, $\widetilde{\mathbf{B}}^{\mathbf{pp}}$ depend on the derivatives of the shape functions and the scaling and attenuation functions of the PML, and the matrices $\widetilde{\mathbf{B}}$, $\mathbf{B}^{\boldsymbol{\varepsilon}}$ and $\mathbf{B}^{\mathbf{Q}}$ are derived by assuming approximate relationships between the time derivatives and time integrals of the stresses and strains. Finally, the internal force can be decomposed in two parts: the first part is related to the previous PML matrices $\tilde{\mathbf{C}}^\mathbf{e}$ and $\widetilde{\mathbf{K}}^\mathbf{e}$, operating on velocities and displacements and the second part, $\mathbf{P_2}\left(\boldsymbol{\varepsilon}_\mathbf{j-1}, \mathbf{E}_\mathbf{j-1}, \boldsymbol{\Sigma}_\mathbf{j-1}, \widetilde{\boldsymbol{\Sigma}}_\mathbf{j-1}\right)$, corresponds to the part of the internal force known at the beginning of the fine time step.

The equations of motion in Eq. (14) and Eq. (15) are complemented with the velocity continuity condition in Eq. (12), written at the fine time scale:

$$\mathbf{L_1 \dot{U}_1^j} + \mathbf{L_2 \dot{U}_2^j} = \mathbf{0} \tag{22}$$

Subdomain Ω_1 is integrated in time with a Newmark explicit scheme ($\beta_1 = 0$ and $\gamma_1 = 1/2$) [40], with a lumped mass matrix M_1. We define $\mathbf{U_1^{0,p}}$ as the predictor of the displacement and $\mathbf{\dot{U}_1^{0,p}}$

as the predictor of the velocity, which is classically introduced in the approximate Newmark formulas as:

$$\mathbf{U_1^{0,p}} = \mathbf{U_1^0} + \Delta t \dot{\mathbf{U}}_\mathbf{1}^\mathbf{0} + \left(\frac{1}{2} - \beta_1\right)\Delta t^2 \ddot{\mathbf{U}}_\mathbf{1}^\mathbf{0} \tag{23}$$

$$\dot{\mathbf{U}}_\mathbf{1}^\mathbf{0,p} = \dot{\mathbf{U}}_\mathbf{1}^\mathbf{0} + \frac{1}{2}\Delta t(1-\gamma_1)\ddot{\mathbf{U}}_\mathbf{1}^\mathbf{0} \tag{24}$$

The classical approximate Newmark formulas in terms of the displacements and velocities at the end of the time step t_j are expressed in acceleration format as below:

$$\mathbf{U_1^m} = \mathbf{U_1^{0,p}} + \beta_1 \Delta t^2 \ddot{\mathbf{U}}_\mathbf{1}^\mathbf{m} \tag{25}$$

$$\dot{\mathbf{U}}_\mathbf{1}^\mathbf{m} = \dot{\mathbf{U}}_\mathbf{1}^\mathbf{0,p} + \gamma_1 \Delta t \ddot{\mathbf{U}}_\mathbf{1}^\mathbf{m} \tag{26}$$

In explicit computation, the final displacement $\mathbf{U_1^m}$ is known at the beginning of the time step because $\beta_1 = 0$. The final acceleration vector $\ddot{\mathbf{U}}_\mathbf{1}^\mathbf{m}$ has to be computed in order to update the final velocity vector $\dot{\mathbf{U}}_\mathbf{1}^\mathbf{m}$.

Concerning the subdomain Ω_2, we use a Central Difference scheme with the terms related to velocities written at the mid time step $(\mathbf{C_2} + \tilde{\mathbf{C}}_\mathbf{2})\dot{\mathbf{U}}_\mathbf{2}^{\mathbf{j-1/2}}$, as classically assumed for explicit time integration in order to avoid system solving [36] and to keep a diagonal mass matrix. The explicit approximate updating formulas of the Central Difference explicit scheme for subdomain Ω_2 are expressed as:

$$\dot{\mathbf{U}}_\mathbf{2}^{\mathbf{j-1/2}} = \dot{\mathbf{U}}_\mathbf{2}^{\mathbf{j-3/2}} + \Delta \mathrm{t}\, \ddot{\mathbf{U}}_\mathbf{2}^{\mathbf{j-1}} \tag{27}$$

$$\mathbf{U}_\mathbf{2}^\mathbf{j} = \mathbf{U}_\mathbf{2}^{\mathbf{j-1}} + \Delta \mathrm{t}\, \dot{\mathbf{U}}_\mathbf{2}^{\mathbf{j-1/2}} \tag{28}$$

$$\bar{\mathbf{U}}_\mathbf{2}^\mathbf{j} = \bar{\mathbf{U}}_\mathbf{2}^{\mathbf{j-1}} + \Delta \mathrm{t} \mathbf{U}_\mathbf{2}^\mathbf{j} \tag{29}$$

All the above quantities are known at the beginning of the time step, at the time t_{j-1}. It remains to compute the acceleration $\ddot{\mathbf{U}}_2^{\mathbf{j}}$ at the end of the time step, and the following mid step velocity being computed by: $\dot{\mathbf{U}}_2^{\mathbf{j+1/2}} = \dot{\mathbf{U}}_2^{\mathbf{j-1/2}} + \Delta t\, \ddot{\mathbf{U}}_2^{\mathbf{j}}$.

Finally, by introducing the above approximate formulas for time integration into Eqs. (14) and (15), it leads to the set of equations of motion, complemented with the velocity continuity relationship, whose unknowns to be solved are the acceleration, written as:

$$\begin{cases} \mathbf{M_1}\ddot{\mathbf{U}}_1^{\mathbf{m}} = \mathbf{F}_1^{\mathbf{ext,m}} - \mathbf{K_1}\mathbf{U}_1^{\mathbf{0,p}} - \mathbf{L}_1^{\mathbf{T}}\boldsymbol{\lambda}^{\mathbf{m}} \\ \mathbf{M_2}\ddot{\mathbf{U}}_2^{\mathbf{j}} = -\mathbf{P}_2\left(\boldsymbol{\varepsilon}_{\mathbf{j-1}}, \mathbf{E}_{\mathbf{j-1}}, \boldsymbol{\Sigma}_{\mathbf{j-1}}, \tilde{\boldsymbol{\Sigma}}_{\mathbf{j-1}}\right) - \left(\mathbf{C_2} + \tilde{\mathbf{C}}_2\right)\dot{\mathbf{U}}_2^{\mathbf{j-1/2}} - \left(\mathbf{K_2} + \tilde{\mathbf{K}}_2\right)\mathbf{U}_2^{\mathbf{j}} - \bar{\mathbf{K}}_2\bar{\mathbf{U}}_2^{\mathbf{j}} - \mathbf{L}_2^{\mathbf{T}}\boldsymbol{\lambda}^{\mathbf{j}} \\ \mathbf{L_1}\dot{\mathbf{U}}_1^{\mathbf{j}} + \mathbf{L_2}\dot{\mathbf{U}}_2^{\mathbf{j}} = \mathbf{0} \end{cases} \quad (30)$$

As classically done for explicit dynamics, we assume a lumped mass matrix in the PML subdomain Ω_2. It enables us to carry out a complete explicit computation in the PML subdomain, leading to an important gain in terms of the computation time, which is particularly suitable for large 3D problems. It will be shown in numerical applications that the CFL condition related to the interior subdomain is also valid for the PML subdomain without stability problems.

In Eq. (30), it is important to note that the velocity continuity is prescribed at the end of the fine time step, whereas the velocity is computed at the mid step in the PML subdomain. As a consequence, the final velocity in the velocity continuity equation is calculated as:

$$\dot{\mathbf{U}}_2^{\mathbf{j}} = \dot{\mathbf{U}}_2^{\mathbf{j-1/2}} + \frac{1}{2}\Delta t\, \ddot{\mathbf{U}}_2^{\mathbf{j}} \quad (31)$$

To solve the set of coupled equations in Eq. (30), we first determine the Lagrange multipliers ensuring the velocity continuity at the interface and second, we solve the accelerations in both subdomains. Following the lines of the coupling GC method [37,38], the kinematic quantities are divided into two parts: the free and the linked quantities. The free quantities are calculated by

taking into account the internal and external forces, without considering the interface forces, whereas the linked quantities are obtained from the interface loads given by the Lagrange multiplier vector $\boldsymbol{\lambda}$. It can be demonstrated that the kinematic continuity condition can be expressed as a reduced-size interface problem as follows:

$$\mathbf{H}\boldsymbol{\lambda}^{\mathbf{j}} = \mathbf{b}^{\mathbf{j}} \tag{32}$$

with the interface operator and the right-hand side member vector defined by:

$$\begin{cases} \mathbf{H} = \gamma_1 \Delta t_1 \mathbf{L_1} \mathbf{M_1}^{-1} \mathbf{L_1^T} + \gamma_2 \Delta t_2 \mathbf{L_2} \mathbf{M_2}^{-1} \mathbf{L_2^T} \\ \mathbf{b}^{\mathbf{j}} = \mathbf{L_1} \dot{\mathbf{U}}_{\mathbf{1}}^{\mathbf{free,j}} + \mathbf{L_2} \dot{\mathbf{U}}_{\mathbf{2}}^{\mathbf{free,j}} \end{cases} \tag{33}$$

The interface operator **H** is called the Steklov-Poincaré operator which can be viewed as the condensed mass matrix with the degrees of freedom belonging to the interface between the two subdomains. The right hand-side vector $\boldsymbol{b^j}$ only depends on the free velocities computed in both subdomains without considering the interface forces; it can be seen as a predictor value projected to the degrees of freedom belonging to the interface.

Finally, once derived the Lagrange multiplier vector $\boldsymbol{\lambda}^{\mathbf{j}}$, the quantities related to the interface forces in the second equation of the set of equations in Eq. (30) can be computed, and the fine time step $\Delta t_2 = [t_{j-1}; t_j]$ is completed by summing these linked quantities with the previously obtained free quantities. Same procedure is applied for every fine time steps Δt_2, by looping over the large time step $\Delta t_1 = [t_0; t_m]$. The last Lagrange multiplier $\boldsymbol{\lambda^m}$ over the large time step allows to complete the large time step and then we can proceed to the next large time step Δt_1.

2.4 Absorbing Layers with Increasing Damping using Rayleigh and Kosloff damping

In the finite element setting, it can be much more convenient to employ different damping formulations from the PML. For instance, Rayleigh damping is classically available in FE code.

Recently, Kosloff damping was investigated for 2D problems and turned out to be suitable for modeling unbounded domains, due to its frequency independent feature [16]. Here, the explicit PML discussed previously will be compared to the cases of Absorbing Layers with Increasing Damping (ALID) using Rayleigh and Kosloff damping, by extending AILD to the 3D case. The explicit framework explained before is employed again.

In the case of Rayleigh damping, the coupling problem, discretized in space and time, can be written as:

$$\begin{cases} \mathbf{M_1}\ddot{\mathbf{U}}_1^{\mathbf{m}} = \mathbf{F}_1^{\mathbf{ext,m}} - \mathbf{K_1}\mathbf{U}_1^{\mathbf{0,p}} - \mathbf{L}_1^{\mathbf{T}}\boldsymbol{\lambda}^{\mathbf{j}} \\ \mathbf{M_2}\ddot{\mathbf{U}}_2^{\mathbf{j}} = -\mathbf{C}_{\mathbf{2,Rayleigh}}\dot{\mathbf{U}}_2^{\mathbf{j-1/2}} - \mathbf{K_2}\mathbf{U}_2^{\mathbf{j}} - \mathbf{L}_2^{\mathbf{T}}\boldsymbol{\lambda}^{\mathbf{j}} \\ \mathbf{L_1}\dot{\mathbf{U}}_1^{\mathbf{j}} + \mathbf{L_2}\dot{\mathbf{U}}_2^{\mathbf{j}} = \mathbf{0} \end{cases} \tag{34}$$

where the Rayleigh matrix is linearly dependent on the mass and stiffness matrix, as:

$$\mathbf{C_{2,Rayleigh}} = \alpha_M \mathbf{M_2} + \alpha_K \mathbf{K_2} \tag{35}$$

In the case of Kosloff damping, the governing discrete coupling problem is given by:

$$\begin{cases} \mathbf{M_1}\ddot{\mathbf{U}}_1^{\mathbf{m}} = \mathbf{F}_1^{\mathbf{ext,m}} - \mathbf{K_1}\mathbf{U}_1^{\mathbf{0,p}} - \mathbf{L}_1^{\mathbf{T}}\boldsymbol{\lambda}^{\mathbf{j}} \\ \mathbf{M_2}\ddot{\mathbf{U}}_2^{\mathbf{j}} = -\mathbf{C}_{\mathbf{2,Kosloff}}\dot{\mathbf{U}}_2^{\mathbf{j-1/2}} - \widetilde{\mathbf{K}}_{\mathbf{2,Kosloff}}\mathbf{U}_2^{\mathbf{j}} - \mathbf{K_2}\mathbf{U}_2^{\mathbf{j}} - \mathbf{L}_2^{\mathbf{T}}\boldsymbol{\lambda}^{\mathbf{j}} \\ \mathbf{L_1}\dot{\mathbf{U}}_1^{\mathbf{j}} + \mathbf{L_2}\dot{\mathbf{U}}_2^{\mathbf{j}} = \mathbf{0} \end{cases} \tag{36}$$

where the Kosloff matrices are defined by summing over the elements as:

$$\mathbf{C_{2,Kosloff}} = \sum 2 \int_{\Omega_e} \rho\gamma \quad [\mathbf{N}]^{\mathbf{T}}[\mathbf{N}] d\Omega \tag{37}$$

$$\widetilde{\mathbf{K}}_{\mathbf{2,Kosloff}} = \sum \int_{\Omega_e} \rho\gamma^2 [\mathbf{N}]^{\mathbf{T}}[\mathbf{N}] d\Omega. \tag{38}$$

2.5 Design of the PML and of the ALID using Rayleigh and Kosloff damping

At the interface, it is well known that the PML is completely reflectionless in theory [17]. Nonetheless, this property is only valid in the continuous setting. Indeed, although there is analytically no reflection at the interface, the spatial discretization will introduce spurious reflections at the interface, so optimal PML's parameters need to be applied in order to minimize these numerical reflections. The real-valued positive functions should monotonically increase and vanish at the interface so that the contrast is minimized, in the discrete setting, between the physical domain and the unphysical PML. Classically, the damping function f^p is written as a polynomial of degree n as shown below [23,24,25, 29, 41]:

$$\beta(x) = \beta_0 \left(\frac{x - x_0}{L}\right)^n \tag{39}$$

where β_0 is the user-tunable scalar parameter. In fact, the larger β_0 is, the larger the discretization error becomes. In other words, more spurious reflected waves will be produced at the interface with a larger β_0 value.

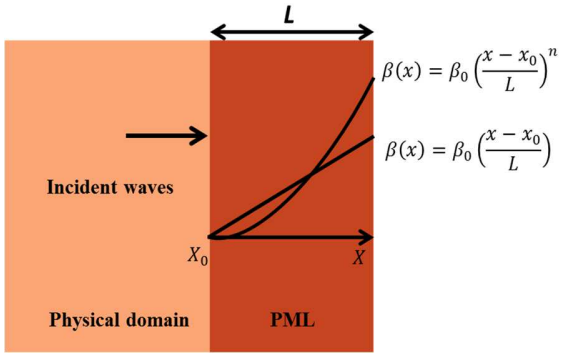

Fig. 2 Evolution of the damping functions in PML subdomain

The logarithmic decrement of PML domain δ is obtained by integrating Eq. (39) over the thickness of the PML:

$$\delta = \int_{x_0}^{L} \frac{\beta_0}{v_\rho} \left(\frac{x - x_0}{L}\right)^n dx = \frac{\beta_0 L}{(n+1)v_\rho} \tag{40}$$

We define the attenuation coefficient $R_{attenution}$ from the logarithmic decrement as:

$$R_{attenuation} = \left(\frac{|u(x+L)|}{|u(x)|}\right)^2 = e^{-2\delta} \tag{41}$$

For instance, if we want to reach a target logarithmic decrement δ=ln (10), it means that 90% of the amplitude of the incident wave is absorbed from the interface to the end of the PML. Next, the attenuation also occurs for the reflection process from the end of the PML towards the interface. Hence, the incident wave is attenuated by 99% and the attenuation coefficient $R_{attenution}$ is theoretically equal to 1% before the space and time discretization.

Finally, we can propose the general formula to design a PML based on the presented 1D harmonic wave problem in PML medium. After choosing the $R_{attenuation}$, the total thickness L and the power n of the damping function, β_0 can be obtained as:

$$\beta_0 = \frac{(n+1)}{2L} \times v_\rho \times \ln\left(\frac{1}{R_{attenuation}}\right) \tag{42}$$

Concerning Kosloff damping, it was shown in Li et al [16] that the scalar-valued γ parameter in Eqs. (37) and (38) can be defined in the same manner as the damping function f^p in Eq. (39), that is: $\gamma(x) = \gamma_0 \left(\frac{x-x_0}{L}\right)^n$. It leads to the same design relationship given by:

$$\gamma_0 = \frac{(n+1)}{2L} \times v_\rho \times \ln\left(\frac{1}{R_{attenution}}\right) \tag{43}$$

It is important to remind that the capability of the ALID with Kosloff damping to damp out incident waves is independent of the frequency and very similar to that of the PML [16]. All the waves with different frequencies can be attenuated in the same way. Nonetheless, at the interface,

the behavior is different in the two cases. Indeed, it is well known that no reflection occurs at the PML interface for all the frequencies. This is not the case for Kosloff damping. This is why optimal conditions have been set up in the work by Li et al [16] for tuning Young's modulus of each Kosloff layer in order to minimize the spurious wave reflections.

Concerning Rayleigh damping, the same polynomial profile for the damping ratio can be considered as that in Eq. (39), that is $\xi(\mathrm{x}) = \xi_0 \left(\frac{x-x_0}{L}\right)^{\mathrm{n}}$ [35] with the assumption $\frac{\alpha_M}{\omega_0} = \alpha_K \omega_0 = \xi$ [15] . For a design angular frequency ω_0 , the design relationship for the ALID based on Rayleigh damping is given by:

$$\xi_0 = \frac{(\mathrm{n}+1)}{2L\omega_0} \times v_\rho \times \ln\left(\frac{1}{R_{attenution}}\right) \tag{44}$$

Here, it can be observed that the design of the Rayleigh ALID introduces a design angular frequency ω_0. In fact, the absorbing ability of Rayleigh damping is dependent on the frequency, which is different from the PML and Kosloff damping. Once the wave propagation model is set up with a suitable finite element size and time step size, depending on the material parameters and characteristics of the input motion, any type of motion (small-band, broad-band) can be investigated using absorbing layers. The most sensitive parameter for the accuracy of the absorbing layer is its thickness, that is, the number of finite elements introduced in the absorbing layer to correctly reproduce the attenuation of the waves.

3 Numerical examples

3.1 Pseudo-3D Lamb's test for PML and ALID comparisons

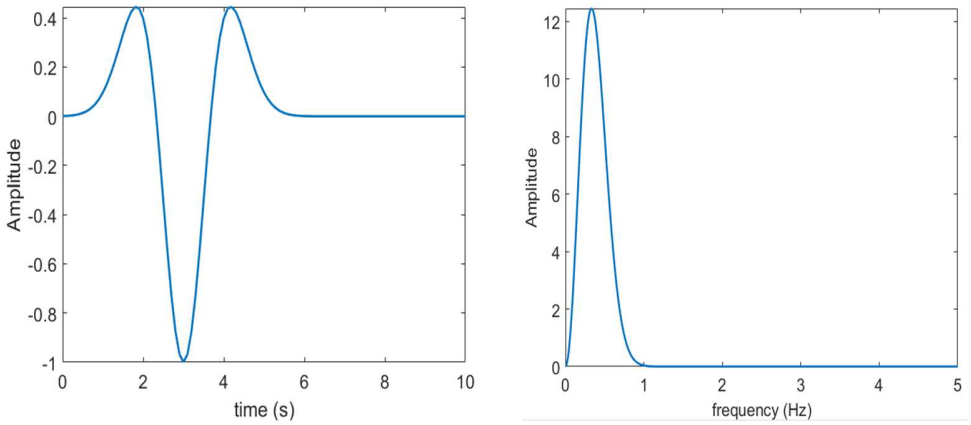

Fig.3 Waveform and Fourier transform of the Ricker wavelet

In order to evaluate the effectiveness of the three-dimensional PML, 3D Lamb's [42] test is carried out. Non-harmonic waves are investigated by considering a Ricker incident wave, defined by:

$$Ric(t, t_p, t_s) = A\left(2\pi^2 \frac{(t-t_s)^2}{t_p^2} - 1\right) \exp\left(-\pi^2 \frac{(t-t_s)^2}{t_p^2}\right) \tag{45}$$

The Ricker wave, plotted in the time domain and in the frequency domain in Fig.3, has three parameters: the fundamental period t_p, the time shift t_s and the amplitude A. The chosen values are: t_p=3 s, t_s=3 s and A =1 MN.

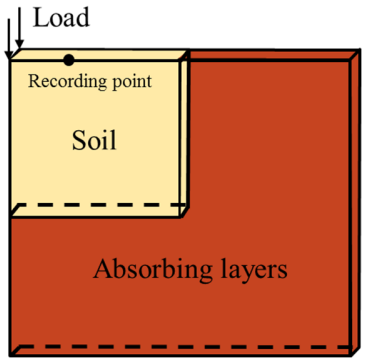

Fig.4 3D Lamb's test using PML and Rayleigh/Kosloff ALID

The test is simulated with only one 3D element in the thickness direction as shown in Fig.4. This thin slice mesh is considered in this first numerical application so as to reduce the computation time in comparison to a full 3D case and to easily compare the performance of the different approaches, the PML, ALID with Rayleigh damping and ALID with Kosloff damping. The Ricker load is applied vertically at the top left edge of the 3D mesh. One recording point is located on the soil surface, at 20 m from the applied load. The soil is assumed to be linear elastic with the dimension 250 m x 250 m x 5 m. All hexahedral finite elements have the dimension 5 m x 5 m x 5 m. The material characteristics for the interior subdomain Ω_1 and the PML subdomain Ω_2 are: ρ_1=1700 kg/m^3, E_1=10 MPa and ν_1= 0.24 for the density, Young's modulus and Poisson's ratio, respectively. The P-wave, S-wave and Rayleigh wave velocities are: V_P =83.27 m/s, V_S=48.7 m/s, V_R=44.73 m/s. The minimal period for the Ricker input can be assessed by the relationship: $T_{min} = 2.5\, t_p$. To achieve sufficient accuracy, the FE size for the linear finite elements, should respect the following relationship: $L_{EF} < \frac{\lambda_{min}}{20}$, with the minimal wavelength λ_{min} equal to $c_P\, T_{min}$. The length L of the PML, also called the thickness in the section 2.5, is taken as equal to 50 m, corresponding to 10 finite elements in the length. The other parameters for the PML design, given in Eq. (42), are the power of polynomial function representing the damping function of the PML and the target attenuation coefficient, given by: $n = 2$ and $R_{attenution} = 0.01$. The subdomain soil is integrated in time by the Newmark explicit scheme without damping and with the time step Δt_1=0.025 s, imposed by the CFL condition, whereas the PML is integrated by the Central Difference scheme, with damping terms written at the mid-step, with the same time step $\Delta t_1 = \Delta t_2$.

The efficiency and accuracy of Rayleigh and Kosloff ALID in modeling three-dimensional unbounded domains are compared with the PML. The ALID is established with a length of 250 m, in order to reduce the reflection at the interface between the interior subdomain and the absorbing subdomain, because they are not reflectionless for all the frequencies. The number of elements in the length of the ALID is thus five times larger than that of the PML, in order to reach a sufficient good accuracy. As shown by Li et al [16], Rayleigh and Kosloff ALID are not reflectionless for all the frequencies, so larger length is mandatory to reduce the damping ratio, based on the design formulas in Eqs. (43) and (44). From this point of view, it is clear that PML is much more efficient than Rayleigh and Kosloff ALID.

The multi-time step capability of the proposed approach is employed in the case of the Rayleigh damping. Indeed, as widely known [36], the stability of the Central Difference scheme with the viscous damping terms is altered by the introduction of Rayleigh damping, leading to the reduction of the critical time step size. As a consequence, it is particularly convenient to adopt an explicit multi-time step strategy in order to satisfy the reduced CFL condition in the Rayleigh ALID while keeping the unchanged CFL condition in the interior subdomain. Here, we adopt a fine time step given by: $\Delta t_1=10\Delta t_2=0.025$ s, which has a time step ratio equal to 10 between the two time steps. For Kosloff ALID, the introduction of Kosloff damping does not alter the critical time step, leading to same time step in the Kosloff ALID as that in the interior subdomain $\Delta t_1 =\Delta t_2$.

In order to assess the accuracy of the PML and ALID methods, the error with respect to the reference results obtained from an extended mesh, free of spurious reflected waves coming from the boundaries of the truncated mesh, is computed as:

$$\text{error}(\%) = \frac{\max_n \left| u_p(t_n) - u_{ref}(t_n) \right|}{\max_n \left| u_{ref}(t_n) \right|} \tag{46}$$

where u_{ref} and u_p are the displacements of the extended mesh model and the PML model. The above error allows us to quantify the spurious reflections.

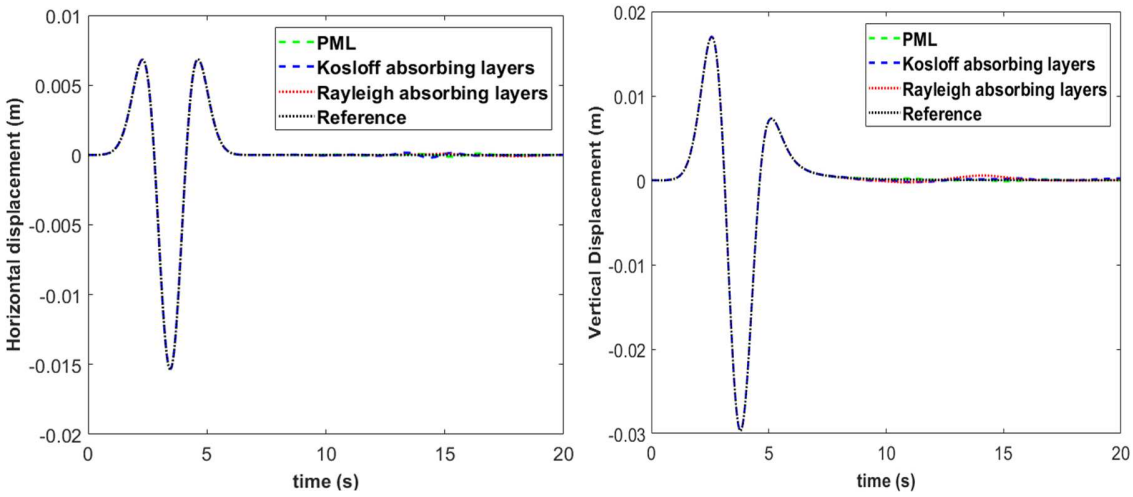

Fig.5 Vertical and horizontal displacements at the recording point using different absorbing layers (the length of the PML is equal to 50 m and the length of Rayleigh and Kosloff ALID is equal to 250 m)

In Fig.5, three absorbing layers are compared in terms of the horizontal displacement and vertical displacement. It can be observed that all the displacements obtained by the three kinds of absorbing layers agree very well with the reference results. Nonetheless, as shown in Table 1, the PML is the most accurate one, with both vertical and horizontal reflections under 1%. The CPU times are resumed in Table 2 in a normalized form divided by the CPU time of Rayleigh absorbing layer, corresponding to the less efficient method. Indeed, Rayleigh ALID has a higher computation time than that of Kosloff ALID, because the time steps in the absorbing region are reduced due to the introduction of the Rayleigh matrix in Central Difference method. The computation time of PML is approximately 4 times less than that of the Rayleigh and Kosloff

ALID, mainly due to its reduced length of 50 m in comparison to 250 m. In more complex three-dimensional numerical simulations, this advantage is even more significant.

Table 1 Displacement errors using different absorbing layers

	Vertical displacement	Horizontal displacement
PML ($\Delta t_1 = \Delta t_2$)	0.46%	0.82%
Rayleigh-ALID ($\Delta t_1 = 10\Delta t_2$)	1.80%	0.58%
Kosloff-ALID ($\Delta t_1 = \Delta t_2$)	1.26%	0.98%

Table 2 Normalized CPU Time for different absorbing layers

	Rayleigh-ALID	Kosloff-ALID	PML
Normalized CPU time	1	0.76	0.26

It is also interesting to decrease the time step in the PML and in the Kosloff ALID ($\Delta t_1 = 10\ \Delta t_2$, that is a time step ratio m equal to 10), so as to improve the accuracy of the absorbing layers. The time histories of the horizontal displacement and vertical displacement at the recording point are shown in Fig.6, using $\Delta t_1 = 10\ \Delta t_2$ in the three absorbing layers. It is obvious, as observed in Table 3, that a better accuracy is achieved at the expense of the computation time as given in Table 4. Using a fine time step, the PML takes longer time than the Rayleigh and Kosloff ALID, because the computation time related to one FE, integrated over one time step, in the PML, is bigger than the one in Rayleigh and Kosloff ALID.

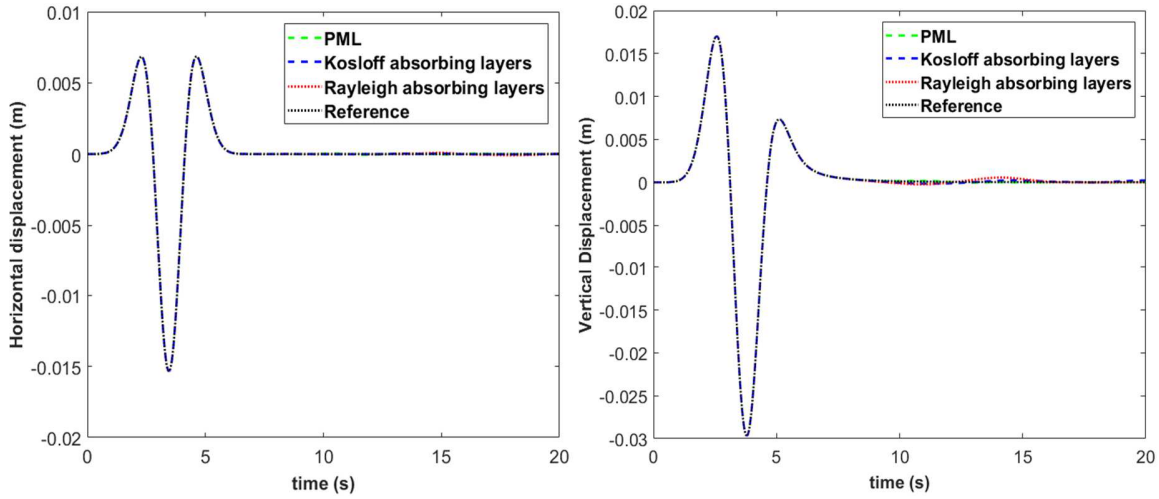

Fig.6 Vertical and horizontal displacements at the observation point using different absorbing layers (m=10, the length of the PML is equal to 50m and the length of the Rayleigh and Kosloff ALID is equal to 250 m)

Table 3 Displacement errors using different absorbing layers (m=10)

	Vertical displacement	Horizontal displacement
PML ($\Delta t_1 = 10\Delta t_2$)	0.29%	0.32%
Rayleigh-ALID ($\Delta t_1 = 10\Delta t_2$)	1.80%	0.58%
Kosloff-ALID ($\Delta t_1 = 10\Delta t_2$)	0.82%	0.21%

Table 4 Normalized CPU time for different absorbing layers (m=10)

	Rayleigh-ALID	Kosloff-ALID	PML
Normalized CPU time	1	0.84	1.59

Owing to the frequency-independence of the damping in the PML and its reflectionless feature at the interface, the PML achieves the best accuracy and computation efficiency when adopting the same time step as the interior domain, confirming that it is the most efficient method to model unbounded domain in a three-dimensional simulation among the three investigated absorbing layers. Finally, to further illustrate the advantage of the reflectionless feature of the PML at the interface, Rayleigh and Kosloff absorbing layers are established with a length of 50 m, which is the same as that of the PML (10 elements in the length). In Fig.7, it can be seen that significant reflections are produced at the interface between the soil subdomain and the Rayleigh and Kosloff ALID. Although optimal conditions at the interface are employed to reduce the reflection at the interface for Rayleigh and Kosloff ALID, the size of the ALID still needs to be longer than that of the PML, because they are not reflectionless for all the frequencies. In the following application focused on the wave barrier, only the PML strategy with a time step ratio m equal to 1, is considered.

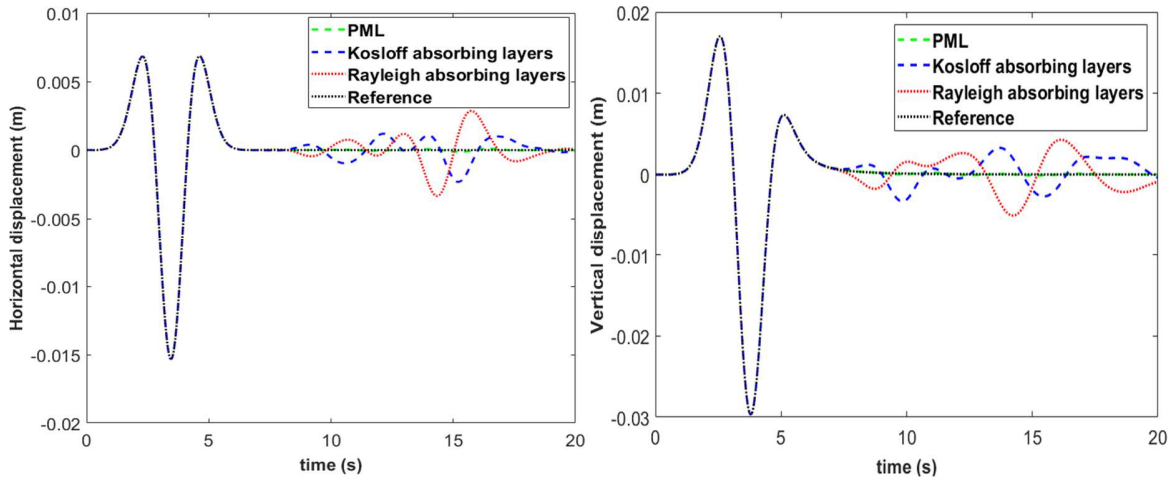

Fig.7 Vertical and horizontal displacements at the recording point using different absorbing layers (the length of thr three absorbing layersis equal to 50m)

3.2 Influence of the PML length: 3D Bar test

As discussed in section 2.5, although the PML is analytically completely reflectionless, the spatial discretization introduces spurious reflections at the interface. For this reason, the length of the PML also has an influence on the accuracy. Because we assume a fixed size of the finite element in the PML, which is given by the material parameters (wave velocity) and the type of FE (shape function), the increase of PML length corresponds to an increase in the number of FEs in the PML.

In order to investigate the influence of the PML length, the case of a semi-infinite elastic bar, subjected to horizontal displacement at the free end, is considered, as shown in Fig.8. The same material parameters as in the previous Lamb's tests are employed. The model is composed of a soil subdomain of 300 m and a PML subdomain with n = 2 and $R_{attenution} = 0.01$. Thus, it simulates the propagation of a P-wave from a non-dissipative elastic medium to a PML medium. Different PML lengths from 10m to 300 m are investigated and the size of FE is the same as that in the Lamb's test (i.e., 5 m x 5 m x 5 m). The observation point C is located at 20 m from the left end of the model.

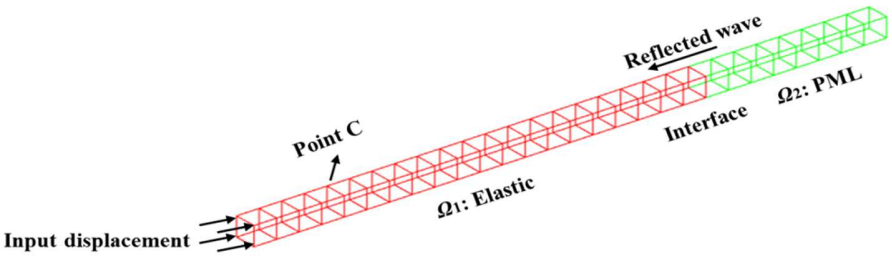

Fig.8 Semi-infinite elastic 3D bar subjected to horizontal displacement

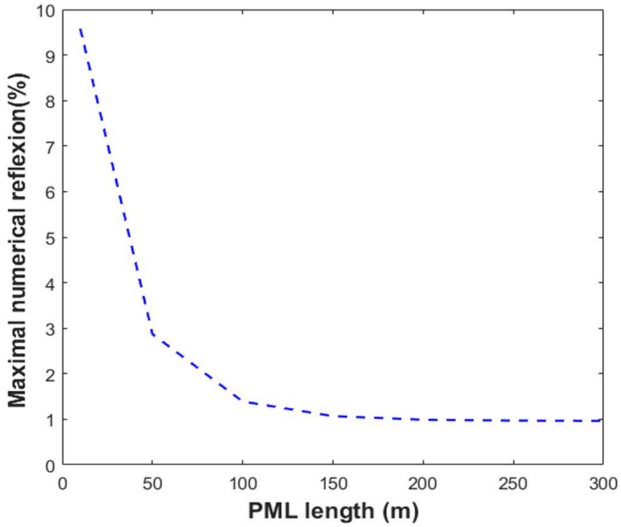

Fig.9 Maximal numerical reflection coefficient as a function of PML length

In Fig.9, the maximum numerical reflection is plotted as a function of the PML length. It is obvious that with a larger length, the maximal numerical reflection coefficient decreases, and better accuracy can be achieved. Indeed, the larger the length is, the more elements there are in the PML to describe the attenuation of the waves, so less spurious reflection is produced at the interface between the soil and the PML subdomain.

3.3 Lamb's test with explicit 3D PML

In order to evaluate the effectiveness of the proposed PML, a more realistic Lamb's test is simulated with the same dimensions in the two horizontal directions as displayed in Fig.10. The numerical model is a quarter model of a PML-truncated semi-infinite homogeneous media subjected to a concentrated force. It is composed of a bounded soil (subdomain 1) with a size of 100 m and PML (subdomain 2) with a thickness of 50 m. The same material characteristics as before are adopted. Non-harmonic waves are investigated by considering a Ricker incident waves with the chosen parameters t_p=3 s, t_s=3 s and A =2 MN. The same size of the eight-node hexahedral element of 5 m x 5 m x 5 m has been taken into account so as to control the inherent

546 wave dispersion. The reference results are computed from an extended mesh. The PML design
547 employed the previous parameters: n is equal to 2 and $R_{attenution}$ is equal to 0.01. A recording
548 point is located on the surface of the subdomain soil at 20 m from each symmetric side. The
549 subdomain soil is integrated in time by Newmark explicit scheme with the time step (Δt_1=0.025
550 s), and the PML is integrated by the Central Difference scheme with the same time step $\Delta t_2=\Delta t_1$,
551 imposed by the condition CFL.

552

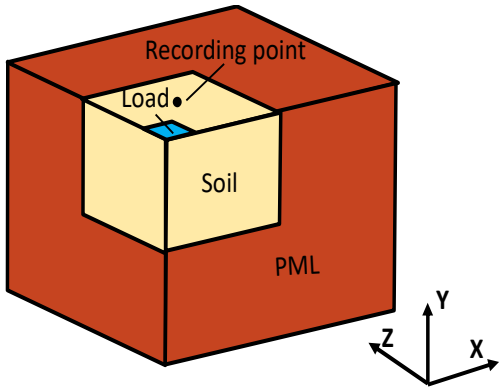

553

554 Fig.10 3D Lamb's test modeled using PML: quarter model of a PML-truncated semi-infinite
555 homogeneous media subjected to a concentrated force

556

557 In Fig.11, we can observe that the displacements for this 3D case are in very good agreement
558 with respect to the reference results: as given in Table 5, the reflected spurious wave is 0.68% in
559 X and Z directions, and 1.24% in Y direction. In the framework of HATI, the interior domain is
560 handled by the classical finite element formulation and Newmark explicit time integrator, instead
561 of introducing complex-coordinate-stretched equations, whereas the PML subdomain is handled
562 by the Central Difference scheme, in order to make use of the diagonal ("lumped") mass matrix
563 of the subdomain Ω_2. Taking into account its advantages in accuracy and CPU time, the proposed

three-dimensional explicit PML is efficient for complex three-dimensional wave propagation simulation. In next section, the PML is applied in the study of the screening effect provided by a horizontal wave barrier in mitigating ground surface vibration generated by an excited plate.

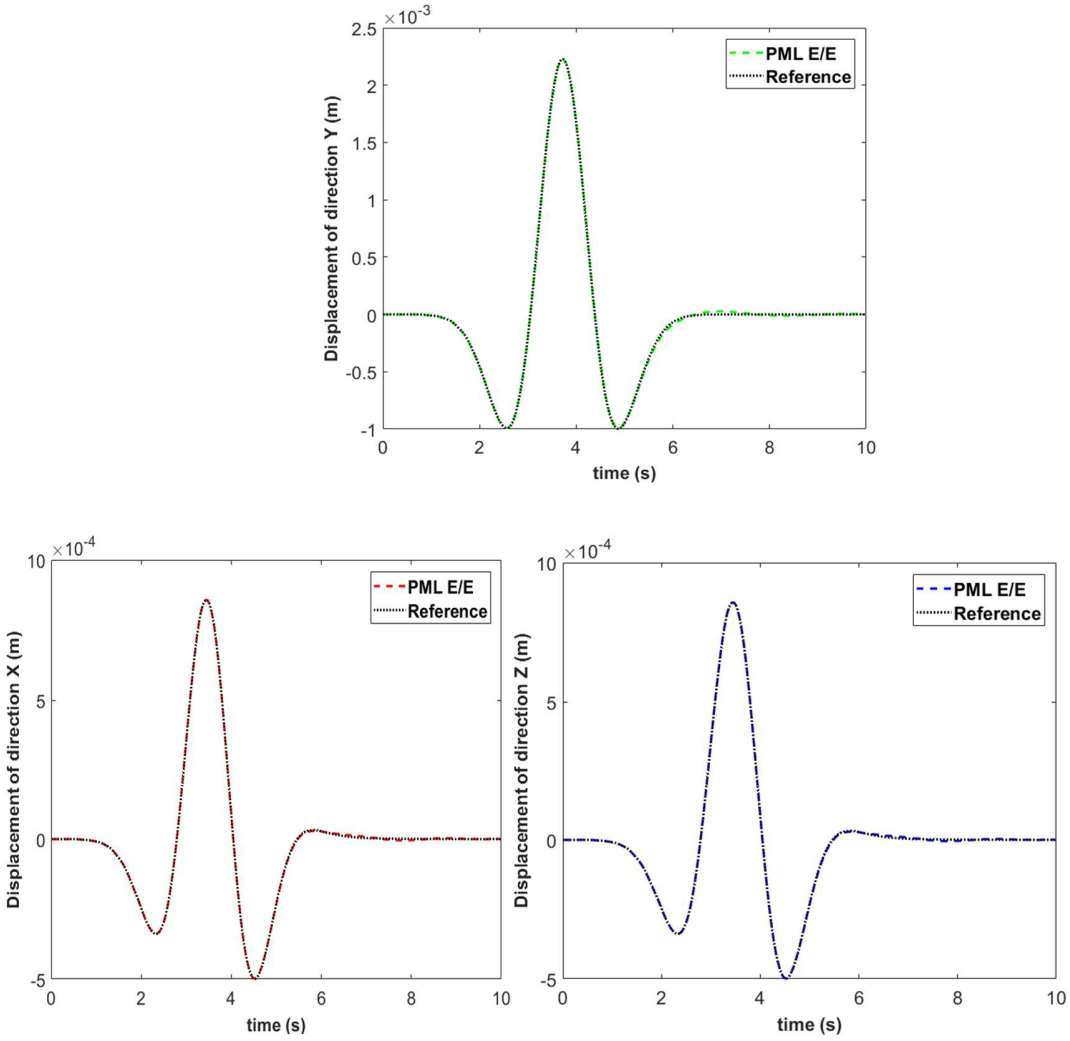

Fig.11 Displacements recorded at the observation point using co-simulation explicit/explicit. (top graph: Y displacement; bottom-left: Z displacement; bottom-right: X displacement)

Table 5 PML displacement errors in different directions with larger soil subdomain

	Displacement X	Displacement Y	Displacement Z

PML	0.68%	1.24%	0.68%

573

574 **3.4 Horizontal Wave Barrier efficiency with explicit 3D PML**

575 Due to the increasing vibrations caused by human activities, the performance of wave
576 barriers for reducing the distress to adjacent structures and annoyance to people, have been
577 studied for more than 30 years. To further demonstrate the efficiency of the proposed approach
578 for modeling unbounded domains, a three-dimensional application is carried out concerning a
579 Horizontal Wave Barrier (HWB), in the context of vibration isolation against the ground surface
580 wave propagation produced by trains and tramways [34]. In this case, the major part of the
581 vibration energy is transferred by Rayleigh waves which may cause strong ground motions on
582 nearby structures [3,4].

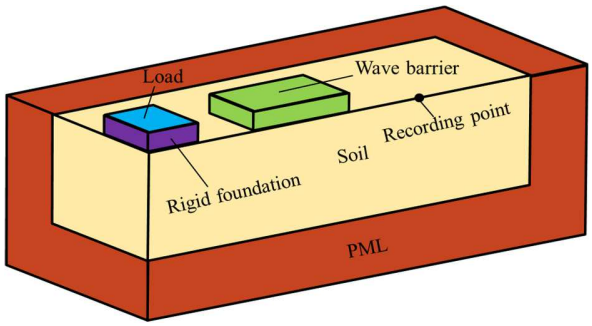

583

584 Fig.12 Configuration of the numerical model of three-dimensional wave barrier problem

585

586 As illustrated in Fig.12, the numerical model is composed of the bounded soil, the PML, the
587 rigid foundation and the horizontal wave barrier. The bounded soil (40 m x 8 m x 8 m) is
588 assumed to be linear elastic with the following material characteristics: ρ_1 =1200 kg/m3,
589 E_1=187.5 MPa and ν_1= 0.25. In the soil, the P-wave, S-wave and Rayleigh-wave velocities are:
590 V_P =433 m/s, V_S=250 m/s, and V_R=230 m/s. The PML is established with the thickness of 4m in

591 the three directions around the bounded soil, with the following parameters: n is equal to 2 and
592 $R_{attenution}$ is equal to 0.01. The rigid foundation on the soil is characterized by a thickness of 0.5
593 m, a surface of 2 m x 2 m, ρ_3=1200 kg/m3, ν_3= 0.25 and E_3=100$E_{1,}$ which is 100 times bigger
594 than Young's modulus in the soil subdomain. The dynamic periodic load, imposed on every node
595 of the rigid foundation surface in the numerical model, is defined by: $P = P_0\sin(\omega_0 t)$, ω_0=2πf_0,
596 P_0=500 kN, f_0=30 Hz. The wavelength for P-wave, S-wave and Rayleigh-wave velocities are
597 14.43 m, 8.33 m, 7.67 m, respectively.

598 For the horizontal wave barrier, D represents the depth of the barrier, W is the width of the
599 barrier, L is the length of the barrier. The horizontal wave barrier is installed behind the rigid
600 foundation with a distance equal to 2 m. The distance from the rigid foundation to the point of
601 interest is 30 m. The material parameters of the HWB are the same as those of the rigid
602 foundation. The isolation effect of the installation of the HWB can be assessed by the parameter
603 A_r (amplitude reduction ratio), which provides a quantitative evaluation of the screening effect of
604 the barrier. Its expression is given by: $A_r = A_b/A_s$, where A_b is the displacement amplitude with
605 the barrier and A_s the displacement amplitude without the barrier. For example, A_r = 0.8 implies
606 that 20% reduction of the vibration has been reached due to the installation of the barrier. The
607 screening effect of the HWB is studied by considering various geometric parameters, such as the
608 length L, the width W and the depth of the barrier D.

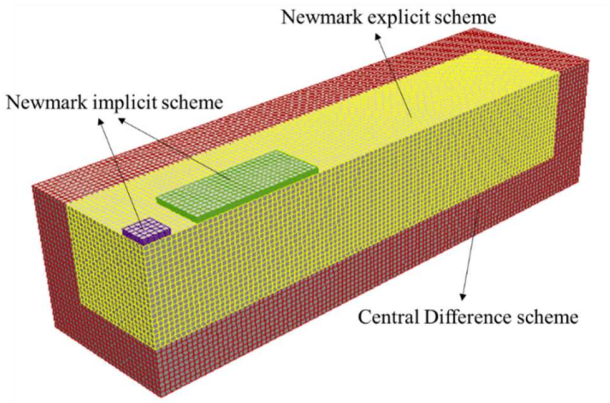

609

610 Fig.13 Different time integration schemes for different subdomains

611

612 Because of the different material characteristics of the coupled problem, the co-simulation
613 strategy will be applied to satisfy the requirement of each part to achieve the best computation
614 efficiency. The numerical model is divided into four subdomains: the bounded soil subdomain,
615 the PML subdomain, the rigid foundation subdomain and the HWB subdomain. Explicit time
616 integration schemes are used to simulate the wave propagation in the soil and PML subdomains
617 as explained previously. Here, the Young's modulus of the rigid foundation and the horizontal
618 wave barrier is 100 times larger than that in the soil subdomain. Consequently, the time step
619 satisfying the CFL condition imposed by the mechanical properties of the rigid foundation should
620 be 10 times smaller than the time step required in soil subdomain. As a result, to avoid reducing
621 the time step, it has been chosen to treat the rigid foundation and HWB subdomains with an
622 unconditionally stable implicit Newmark time integration scheme (Constant Average
623 Acceleration scheme) as proposed in Brun et al. [31]. The four subdomains are coupled by GC
624 coupling algorithm to perform explicit/implicit co-simulation. Fig.13 shows the discretization of
625 the numerical model. To summarize, the three-dimensional horizontal wave barrier problem is
626 divided into four partitions integrated in time with their own time integrator in the most efficient

627 way: soil subdomain (Newmark explicit scheme), barrier subdomain (Newmark implicit scheme),
628 rigid foundation domain (Newmark implicit scheme), and PML (Central Difference scheme). In
629 order to achieve good accuracy in predicting the propagating waves into the soil, the finite
630 element size is kept as 0. 4m x0. 4m x 0. 4m for the soil and PML subdomains and 0.4 m x 0.4
631 mx 0.1 m for the horizontal wave barrier and soil foundation subdomains.

632 The snapshots of the displacement magnitude at different times for the wave propagation
633 simulation are displayed in Fig.14-16, in the case of the HWB with the dimension of 0.5 m x 4 m
634 x 10 m. It is observed that the installation of the horizontal wave barrier efficiently reduces the
635 wave intensity. No obvious reflection can be observed at the interface between the soil
636 subdomain and the PML, demonstrating very satisfactory performance of the PML. In particular,
637 as displayed in Fig. 16 in the end region of this elongated domain, the surface waves travel with
638 respect to the PML interface with a grazing incidence, without visible spurious waves. It
639 indicates a good efficiency of the proposed PML concerning the classical grazing incidence issue,
640 which has been raised in the literature when the classical split PML formulation is adopted [22,43,44,
641 45].

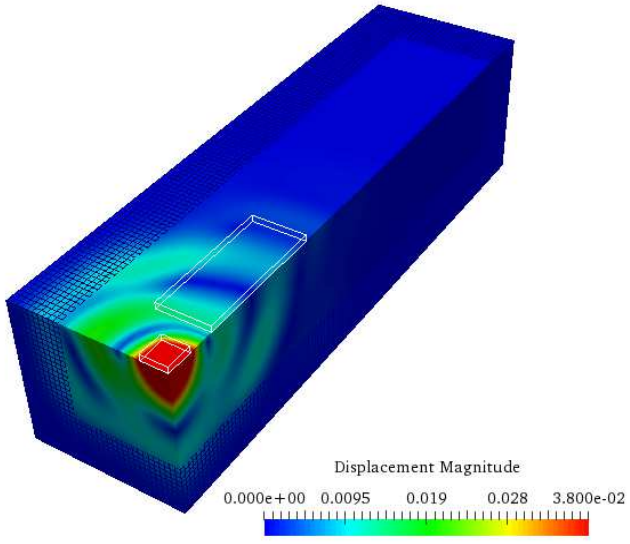

642

Fig.14 Snapshot of displacement magnitude at 0.05 s

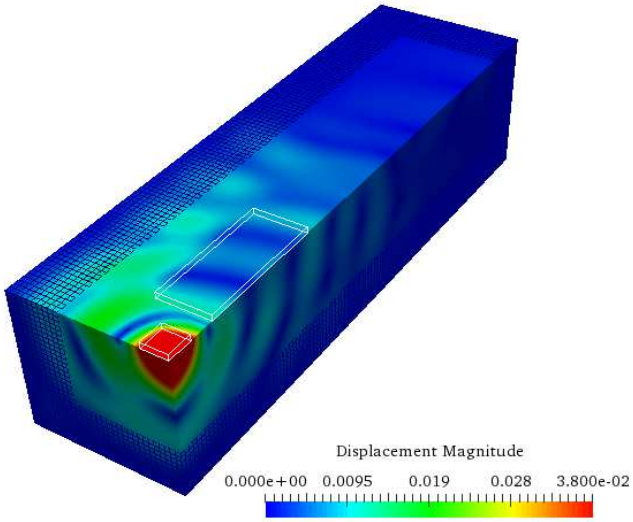

Fig.15 Snapshot of displacement magnitude at 0.1 s

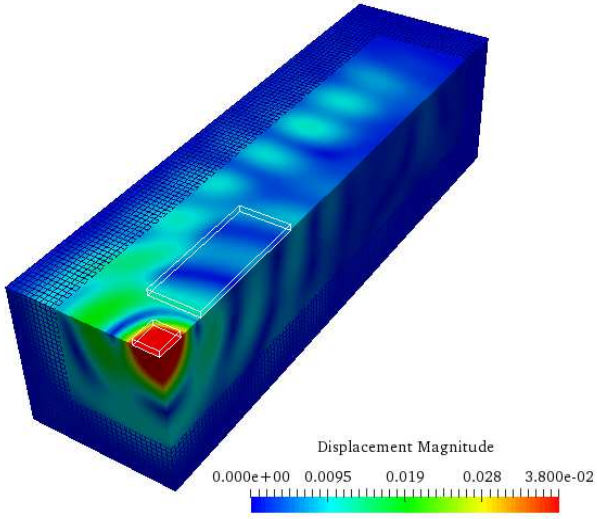

Fig.16 Snapshot of displacement magnitude at 0.15 s

Fig.17 displays the time histories of the displacement at the recording point with different lengths L, compared to the results obtained without barrier. No obvious spurious waves are observed, highlighting the accuracy of the proposed three-dimensional PML. A length L of the

HWB equal to 4m is insufficient to provide a substantial screening effect, whereas 10m and 16m provide significant reductions in displacement.

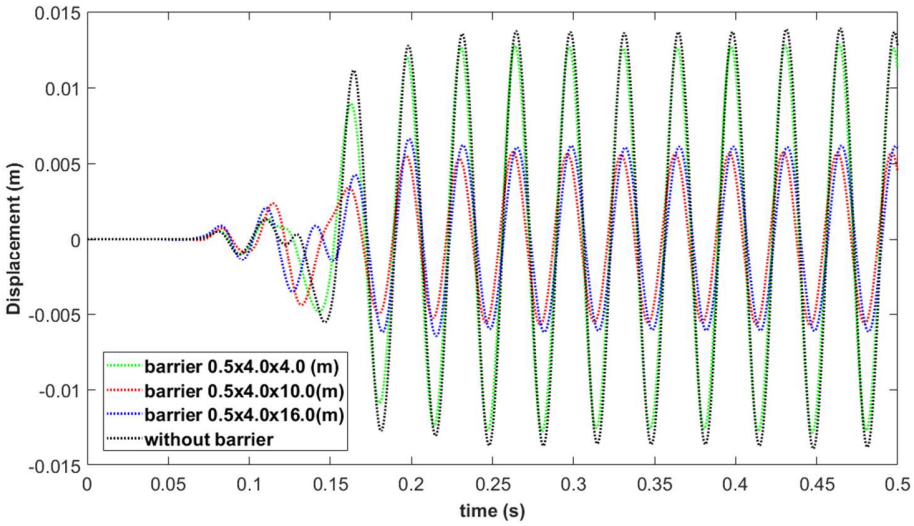

Fig.17 Time histories of the displacement at the recording point in the case of wave barriers with different lengths, compared to the results obtained without barrier.

Concerning the influence of the wave barrier width, which cannot be studied in a simple 2D simulation, we can observe in Fig.18 that, with the same length and depth, wave barriers with the width equal to 4 m can reduce the wave amplitude more efficiently than the wave barriers with the width equal to 2 m. It shows that it is necessary to carry out three-dimensional simulations to thoroughly investigate the isolation effect of wave barriers in realistic situations.

The influence of the wave barrier depth on the isolation effectiveness is also studied. Fig.19 displays the time histories of the displacement at the recording point with two different depths, compared to the results obtained without barrier. With a length equal to 10 m, the HWB is able to provide a significant effect with a depth of 0.5 m. The depth parameter seems less sensitive than the length and width of the HWB.

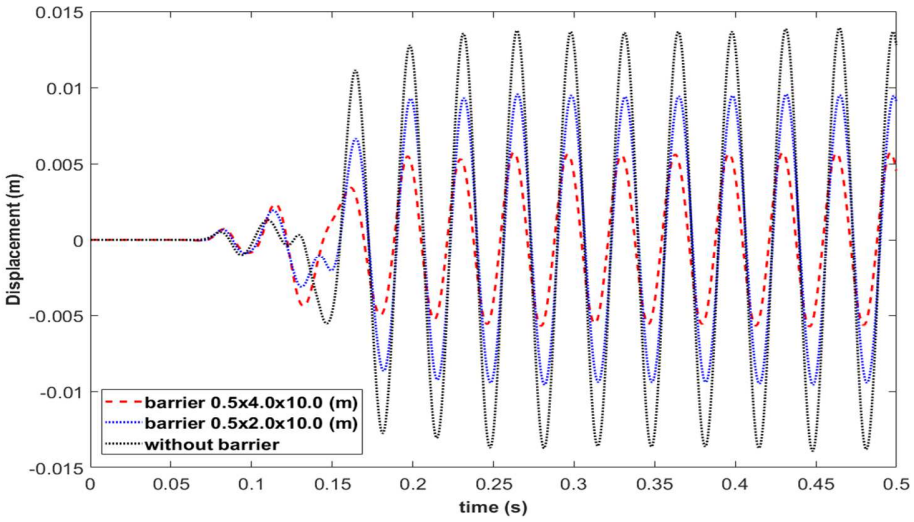

668

669 Fig.18 Time histories of the displacement at the recording point in the case of wave barriers with different

670 widths, compared to the results obtained without barrier

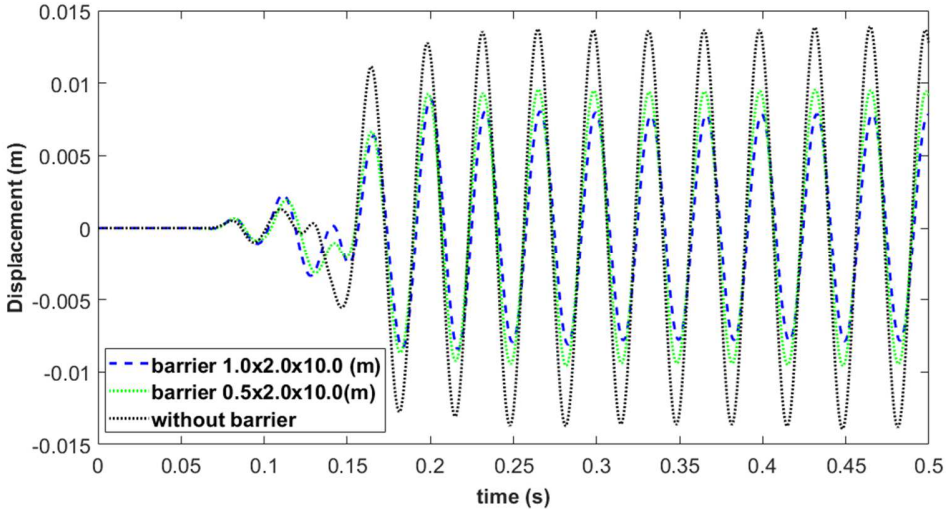

671

672 Fig.19 Time histories of the displacement at the recording point in the case of wave barriers with different

673 depths, compared to the results obtained without barrier.

674

675 Finally, the screening effect of the horizontal wave barrier is investigated with various

676 geometric parameters by plotting, the reduction ratio of the vertical displacement versus the

677 length of the HWB, as shown in Fig.20. It can be seen that the amplitude reduction ratio A_r

678 decreases with the increase of length L. For a length L equal to about 8m, the reduction is optimal.
679 Increasing the length L after this point does not seem to provide a further reduction. In addition, it
680 can be remarked that the width of the HWB also plays an important role, contrarily to the depth
681 of the HWB, which does not provide significant reduction when the depth is increased from 0.5
682 m to 1 m. It has to be reminded that the Rayleigh wave length is equal to 7.67 m which
683 approximately corresponds to the optimal length observed. As remarked in the literature [34], it is
684 well known that the length of HWB should be chosen to be slightly longer than the Rayleigh
685 wavelength to obtain a good isolation effectiveness.

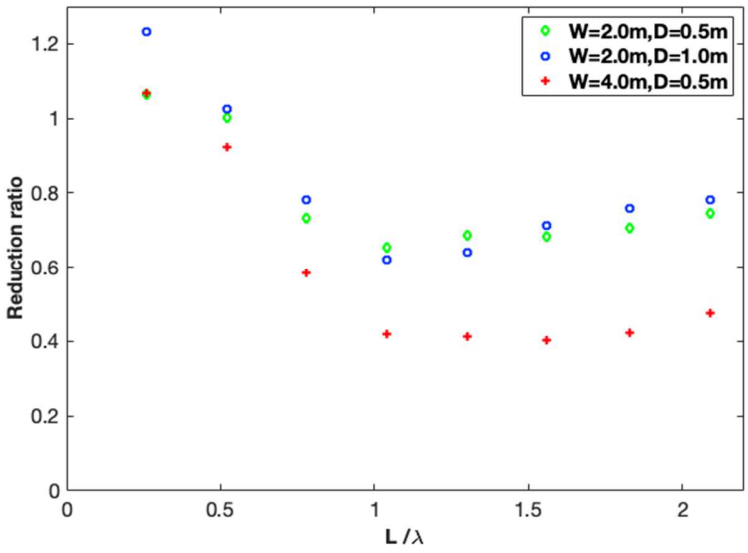

686

687 Fig.20 Reduction ratios of the horizontal wave barrier with various geometric parameters

688

689 **4. Conclusion**

690 A benchmark for three-dimensional explicit asynchronous absorbing layers for modeling
691 unbounded domains is presented. The displacement-based PML making use of the unsplit
692 formulation is integrated using the Central Difference scheme, independently from the interior

693 subdomain, thanks to the versatility of the Heterogeneous (different time integrators)
694 Asynchronous (different time steps) Time Integrator framework. Other absorbing layers, more
695 convenient to be implemented in FE software, are also investigated and compared with the 3D
696 PML: Absorbing Layers with Increasing Damping (ALID) using viscous Rayleigh damping and
697 ALID with Kosloff damping. The introduction of Rayleigh damping in explicit dynamics reduces
698 the time step. As a result, the HATI framework turns out to be very useful for adopting fine time
699 steps in the Rayleigh absorbing layers while keeping the time steps unchanged in the interior
700 domain. In addition, taking fine time steps in the PML and Kosloff-ALID is not mandatory but
701 improves the PML accuracy at the expense of the computation time. The proposed explicit
702 asynchronous 3D PML turns out to be very efficient in terms of the accuracy and computation
703 time: its superiority over Absorbing Layers with Increasing Damping based on Rayleigh and
704 Kosloff damping formulations is highlighted. The PML 3D has been applied to 3D Soil-Structure
705 Interaction problems such as the Lamb's test and the study of the screening effect provided by a
706 horizontal wave barrier set up on the ground for mitigating ground surface vibration induced by
707 an excited plate. Future works are in progress to introduce nonlinear phenomena in the soil of the
708 interior subdomain in complex 3D SSI problems.
709

710 **Appendix A**

711 In the following section, we summarize the matrices expressed as a function of the scaling
712 and attenuation functions f^e and f^p related to the PML.

713 $$\underline{\underline{F}}^e = \begin{bmatrix} 1+f_1^e(x_1) & 0 & 0 \\ 0 & 1+f_2^e(x_2) & 0 \\ 0 & 0 & 1+f_3^e(x_3) \end{bmatrix} \quad \underline{\underline{F}}^p = \begin{bmatrix} f_1^p(x_1) & 0 & 0 \\ 0 & f_2^p(x_2) & 0 \\ 0 & 0 & f_3^p(x_3) \end{bmatrix}$$

$$\underline{\underline{\tilde{F}}}^{ee} = \begin{bmatrix} f_{23}^{ee} & 0 & 0 \\ 0 & f_{13}^{ee} & 0 \\ 0 & 0 & f_{12}^{ee} \end{bmatrix} \quad \underline{\underline{\tilde{F}}}^{ep} = \begin{bmatrix} f_{23}^{ep} & 0 & 0 \\ 0 & f_{13}^{ep} & 0 \\ 0 & 0 & f_{12}^{ep} \end{bmatrix} \quad \underline{\underline{\tilde{F}}}^{pp} = \begin{bmatrix} f_{23}^{pp} & 0 & 0 \\ 0 & f_{13}^{pp} & 0 \\ 0 & 0 & f_{12}^{pp} \end{bmatrix} \tag{A.1}$$

with

$$\begin{cases} f_{ij}^{ee} = [1 + f_i^e(x_i)]\left[1 + f_j^e\left(x_j\right)\right] \\ f_{ij}^{ep} = [1 + f_i^e(x_i)]f_j^p\left(x_j\right) + \left[1 + f_j^e\left(x_j\right)\right]f_i^p(x_i) \\ f_{ij}^{pp} = f_i^p(x_i)f_j^p\left(x_j\right) \end{cases} \tag{A.2}$$

The scalar values involved on the right-hand side member of the equation of motion in Eq. (5) are given below:

$$\begin{cases} f_M = [1 + f_1^e(x_1)][1 + f_2^e(x_2)][1 + f_3^e(x_3)] \\ f_C = [1 + f_1^e(x_1)][1 + f_2^e(x_2)]f_3^p(x_3) + [1 + f_1^e(x_1)][1 + f_3^e(x_3)]f_2^p(x_2) \\ \qquad +[1 + f_2^e(x_2)][1 + f_3^e(x_3)]f_1^p(x_1) \\ f_K = f_1^p(x_1)f_2^p(x_2)[1 + f_3^e(x_3)] + f_2^p(x_2)f_3^p(x_3)[1 + f_1^e(x_1)] \\ \qquad +f_1^p(x_1)f_3^p(x_3)[1 + f_2^e(x_2)] \\ f_H = f_1^p(x_1)f_2^p(x_2)f_3^p(x_3) \end{cases} \tag{A.3}$$

From the weak form of the coupled problem in Eq. (9), the internal force $\mathbf{P_{int}^e}$ related to the PML domain can be written as:

$$\mathbf{P_{int}^e} = \int_{\Omega^e} \tilde{\mathbf{B}}^{\mathbf{eeT}}\hat{\boldsymbol{\sigma}}\mathrm{d}\Omega + \int_{\Omega^e} \tilde{\mathbf{B}}^{\mathbf{epT}}\hat{\boldsymbol{\Sigma}}\mathrm{d}\Omega + \int_{\Omega^e} \tilde{\mathbf{B}}^{\mathbf{ppT}}\hat{\tilde{\boldsymbol{\Sigma}}}\mathrm{d}\Omega \tag{A.4}$$

where the matrices $\tilde{\mathbf{B}}^{\mathbf{ee}}$, $\tilde{\mathbf{B}}^{\mathbf{ep}}$ and $\tilde{\mathbf{B}}^{\mathbf{pp}}$ depend on the derivatives of the shape functions and the scaling and attenuation functions of the PML previously defined. The matrices containing shape function derivatives of 8-node hexahedral element combined with the previous scaling and attenuation functions are expressed as below:

$$\widetilde{\mathbf{B}}_{\mathbf{I}}^{\mathbf{ee}} = \begin{bmatrix} \widetilde{N}_{I1}^{ee} & 0 & 0 \\ 0 & \widetilde{N}_{I2}^{ee} & 0 \\ 0 & 0 & \widetilde{N}_{I3}^{ee} \\ \widetilde{N}_{I2}^{ee} & \widetilde{N}_{I1}^{ee} & 0 \\ \widetilde{N}_{I3}^{ee} & 0 & \widetilde{N}_{I1}^{ee} \\ 0 & \widetilde{N}_{I3}^{ee} & \widetilde{N}_{I2}^{ee} \end{bmatrix} \tag{A.5}$$

$$\widetilde{\mathbf{B}}^{\mathbf{ee}} = [\widetilde{\mathbf{B}}_{\mathbf{1}}^{\mathbf{ee}} \quad \widetilde{\mathbf{B}}_{\mathbf{2}}^{\mathbf{ee}} \quad \cdots \quad \widetilde{\mathbf{B}}_{\mathbf{8}}^{\mathbf{ee}}] \tag{A.6}$$

The components of the above matrices are given for an index $i = 1,2,3$, without the summation convention:

$$\widetilde{N}_{Ii}^{ee} = \tilde{F}_{ii}^{ee} N_{I,i}, \qquad \widetilde{N}_{Ii}^{ep} = \tilde{F}_{ii}^{ep} N_{I,i}, \qquad \widetilde{N}_{Ii}^{pp} = \tilde{F}_{ii}^{pp} N_{I,i} \tag{A.7}$$

$\widetilde{\mathbf{B}}^{\mathbf{ep}}$ and $\widetilde{\mathbf{B}}^{\mathbf{pp}}$ are defined in the same manner as $\widetilde{\mathbf{B}}^{\mathbf{ee}}$, by replacing $\widetilde{N}_{Ii}^{ee}$ with $\widetilde{N}_{Ii}^{ep}$ and $\widetilde{N}_{Ii}^{pp}$, respectively.

The Voigt notation is adopted for the stress and strain tensors, giving the following vectors:

$$\hat{\boldsymbol{\sigma}} = \begin{Bmatrix} \sigma_{11} \\ \sigma_{22} \\ \sigma_{33} \\ \sigma_{12} \\ \sigma_{13} \\ \sigma_{23} \end{Bmatrix} \qquad \hat{\boldsymbol{\varepsilon}} = \begin{Bmatrix} \varepsilon_{11} \\ \varepsilon_{22} \\ \varepsilon_{33} \\ 2\varepsilon_{12} \\ 2\varepsilon_{13} \\ 2\varepsilon_{23} \end{Bmatrix} \tag{A.8}$$

With the constitutive relationship for an isotropic elastic medium:

$$\hat{\boldsymbol{\sigma}} = \mathbf{D}\,\hat{\boldsymbol{\varepsilon}} \tag{A.9}$$

$\mathbf{D}$ is the material constitutive matrix expressed as:

$$\mathbf{D} = \begin{bmatrix} k + 4\mu/3 & k - 2\mu/3 & k - 2\mu/3 \\ k - 2\mu/3 & k + 4\mu/3 & k - 2\mu/3 \\ k - 2\mu/3 & k - 2\mu/3 & k + 4\mu/3 \\ \mu & 0 & 0 \\ 0 & \mu & 0 \\ 0 & 0 & \mu \end{bmatrix} \tag{A.10}$$

For the time stepping procedure over the time step $[t_{j-1}; t_j]$, the following additional relationships are required:

$$\hat{\mathbf{E}}_{\mathbf{j}} = \hat{\mathbf{E}}_{\mathbf{j-1}} + \hat{\boldsymbol{\varepsilon}}_{\mathbf{j-1}}\Delta t, \quad \hat{\boldsymbol{\Sigma}}_{\boldsymbol{j}} = \hat{\boldsymbol{\Sigma}}_{\boldsymbol{j-1}} + \hat{\boldsymbol{\sigma}}_{\mathbf{j-1}}\Delta t, \qquad \hat{\bar{\boldsymbol{\Sigma}}}_{\mathbf{j}} = \hat{\bar{\boldsymbol{\Sigma}}}_{\boldsymbol{j-1}} + \hat{\bar{\boldsymbol{\Sigma}}}\Delta t \tag{A.11}$$

$$\hat{\dot{\boldsymbol{\varepsilon}}}_{\mathbf{j}} = \frac{\hat{\boldsymbol{\varepsilon}}_{\mathbf{j}} - \hat{\boldsymbol{\varepsilon}}_{\mathbf{j-1}}}{\Delta t} \tag{A.12}$$

Using the assumptions given in Eq. (A.12), the third equation of the system in Eq. (7) leads to the expression of the strain $\hat{\boldsymbol{\varepsilon}}_{\mathbf{j}}$ at the end of the time step:

$$\hat{\boldsymbol{\varepsilon}}_{\mathbf{j}} = \frac{1}{\Delta t}\left[\frac{1}{\Delta t}\hat{\mathbf{F}}^{\boldsymbol{\varepsilon}}\hat{\boldsymbol{\varepsilon}}_{\mathbf{j-1}} - \hat{\mathbf{F}}^{\mathbf{Q}}\hat{\mathbf{E}}_{\mathbf{j-1}} + \mathbf{B}^{\boldsymbol{\varepsilon}}\dot{\mathbf{U}}_{\mathbf{j}} + \mathbf{B}^{\mathbf{Q}}\mathbf{U}_{\mathbf{j}}\right] \tag{A.13}$$

The matrices $\hat{\mathbf{F}}^{\boldsymbol{\varepsilon}}$ and $\hat{\mathbf{F}}^{\mathbf{Q}}$, $\mathbf{B}^{\boldsymbol{\varepsilon}}$, $\mathbf{B}^{\mathbf{Q}}$ depend on the derivatives of the shape functions as well as scaling and attenuation functions. We express the $\hat{\mathbf{F}}^{\boldsymbol{\varepsilon}}$ and $\mathbf{B}^{\boldsymbol{\varepsilon}}$ matrices depending on the shape function derivatives as well as scaling and attenuation functions:

$$\hat{\boldsymbol{F}}^{\boldsymbol{\varepsilon}} = \begin{bmatrix} (F_{11}^{\varepsilon})^2 & 0 & 0 & 0 & 0 & 0 \\ 0 & (F_{22}^{\varepsilon})^2 & 0 & 0 & 0 & 0 \\ 0 & 0 & (F_{33}^{\varepsilon})^2 & 0 & 0 & 0 \\ 0 & 0 & 0 & F_{11}^{\varepsilon}F_{22}^{\varepsilon} & 0 & 0 \\ 0 & 0 & 0 & 0 & F_{11}^{\varepsilon}F_{33}^{\varepsilon} & 0 \\ 0 & 0 & 0 & 0 & 0 & F_{22}^{\varepsilon}F_{33}^{\varepsilon} \end{bmatrix} \tag{A.14}$$

$$\boldsymbol{B}^{\boldsymbol{\varepsilon}} = \begin{bmatrix} F_{11}^{\varepsilon}N_{I1}^{l} & 0 & 0 \\ 0 & F_{22}^{\varepsilon}N_{I2}^{l} & 0 \\ 0 & 0 & F_{33}^{\varepsilon}N_{I3}^{l} \\ F_{11}^{\varepsilon}N_{I2}^{l} & F_{22}^{\varepsilon}N_{I1}^{l} & 0 \\ F_{22}^{\varepsilon}N_{I3}^{l} & 0 & F_{33}^{\varepsilon}N_{I1}^{l} \\ 0 & F_{22}^{\varepsilon}N_{I3}^{l} & F_{33}^{\varepsilon}N_{I2}^{l} \end{bmatrix} \tag{A.15}$$

with the matrices:

753 $$\underline{\underline{F}}^{l} = \left[\underline{\underline{F}}^{p} + \frac{\underline{\underline{F}}^{e}}{\Delta t}\right]^{-1} \quad \underline{\underline{F}}^{\epsilon} = \underline{\underline{F}}^{e}\underline{\underline{F}}^{l} \tag{A.16}$$

754 The component in $\boldsymbol{B^{\varepsilon}}$ matrix is given by: $N_{Ii}^{l} = F_{ii}^{l}N_{I,i}$, for $i = 1,2,3$. Finally, $\widehat{\boldsymbol{F}}^{\boldsymbol{\varepsilon Q}}$ and $\boldsymbol{B^{Q}}$

755 are similarly defined, by replacing $\underline{\underline{F}}^{\epsilon}$ with $\underline{\underline{F}}^{Q}$, defined by $\underline{\underline{F}}^{Q} = \underline{\underline{F}}^{p}\underline{\underline{F}}^{l}$.

756 The internal force is decomposed into two parts. The element-wise internal force vector $\mathbf{P_j^e}$

757 can be written in terms of the element velocity $\dot{\mathbf{U}}_{\mathbf{j}}^{\mathbf{e}}$ and displacement vectors $\mathbf{U_j^e}$, related to the end

758 of the time step, as well as a term, denoted by $\mathbf{P}(\boldsymbol{\varepsilon}_{\mathbf{j-1}}^{\mathbf{e}}, \mathbf{E}_{\mathbf{j-1}}^{\mathbf{e}}, \boldsymbol{\Sigma}_{\mathbf{j-1}}^{\mathbf{e}}, \widetilde{\boldsymbol{\Sigma}}_{\mathbf{j-1}}^{\mathbf{e}})$, known at the

759 beginning of the time step. Finally, the element-wise internal force $\mathbf{P_j^e}$ is written as:

760 $$\mathbf{P_j^e} = \left(\int_{\Omega_e} \widetilde{\mathbf{B}}^{\mathbf{T}} \frac{1}{\Delta t}\mathbf{D}\mathbf{B}^{\boldsymbol{\varepsilon}} d\Omega\right)\dot{\mathbf{U}}_{\mathbf{j-1/2}} + \left(\int_{\Omega_e} \widetilde{\mathbf{B}}^{\mathbf{T}} \frac{1}{\Delta t}\mathbf{D}\mathbf{B}^{\mathbf{Q}} d\Omega\right)\mathbf{U_j}$$

761 $$+\mathbf{P}\left(\boldsymbol{\varepsilon}_{\mathbf{j-1}}^{\mathbf{e}}, \mathbf{E}_{\mathbf{j-1}}^{\mathbf{e}}, \boldsymbol{\Sigma}_{\mathbf{j-1}}^{\mathbf{e}}, \widetilde{\boldsymbol{\Sigma}}_{\mathbf{j-1}}^{\mathbf{e}}\right) \tag{A.17}$$

762 with $\mathbf{P}\left(\boldsymbol{\varepsilon}_{\mathbf{j-1}}^{\mathbf{e}}, \mathbf{E}_{\mathbf{j-1}}^{\mathbf{e}}, \boldsymbol{\Sigma}_{\mathbf{j-1}}^{\mathbf{e}}, \widetilde{\boldsymbol{\Sigma}}_{\mathbf{j-1}}^{\mathbf{e}}\right) = \left(\int_{\Omega_e} \widetilde{\mathbf{B}}^{\mathbf{T}} \frac{1}{\Delta t^2}\mathbf{D}\mathbf{F}^{\boldsymbol{\varepsilon}}\boldsymbol{\varepsilon}_{\mathbf{j-1}} d\Omega\right) - \left(\int_{\Omega_e} \widetilde{\mathbf{B}}^{\mathbf{T}} \frac{1}{\Delta t}\mathbf{D}\mathbf{F}^{\mathbf{Q}}\mathbf{E}_{\mathbf{j-1}} d\Omega\right)$

763 $$+\left(\int_{\Omega_e} \widetilde{\mathbf{B}}^{\mathbf{ep}^{\mathbf{T}}}\boldsymbol{\Sigma}_{\mathbf{j-1}}\, d\Omega\right) + \left(\int_{\Omega_e} \widetilde{\mathbf{B}}^{\mathbf{pp}^{\mathbf{T}}}\widetilde{\boldsymbol{\Sigma}}_{\mathbf{j-1}} d\Omega\right) + \left(\int_{\Omega_e} \widetilde{\mathbf{B}}^{\mathbf{pp}^{\mathbf{T}}}\Delta t\, \boldsymbol{\Sigma}_{j-1} d\Omega\right) \tag{A.18}$$

764 and the matrix $\widetilde{\mathbf{B}}$ is defined as a function of the previous matrices $\widetilde{\mathbf{B}}^{\mathbf{ee}}$, $\widetilde{\mathbf{B}}^{\mathbf{ep}}$ and $\widetilde{\mathbf{B}}^{\mathbf{pp}}$ and the time

765 step as follows:

766 $$\widetilde{\mathbf{B}} = \widetilde{\mathbf{B}}^{\mathbf{ee}} + \Delta t\widetilde{\mathbf{B}}^{\mathbf{ep}} + \Delta t^2\, \widetilde{\mathbf{B}}^{\mathbf{pp}} \tag{A.19}$$

767 **References**

768 [1] Schiavia A and Rossib L. Vibration perception in buildings: A survey from the historical

769 origins to the present day. Energy Procedia 2015; 78: 2-7.

770 [2] Çelebi E, Fırat S, Beyhan G, Çankaya İ, Vural İ and Kırtel O. Field experiments on wave
771 propagation and vibration isolation by using wave barriers. Soil Dynamics and Earthquake
772 Engineering 2009; 29: 824–833.
773 [3] Al-Hussaini TM and Ahmad S. Simplified design for vibration screening by open and in-
774 filled trenches. Journal of Geotechnical and Geoenvironmental Engineering 1991; 17(1): 67–88.
775 [4] Beskos DE, Dasgupta B and Vardoulakis IG. Vibration isolation using open or filled trenches,
776 Computational Mechanics 1986; 1: 43-63.
777 [5] Auersch L. Response to harmonic wave excitation of finite or infinite elastic plates on a
778 homogeneous or layered half-space, Computers and Geotechnics 2013; 51; 50-59
779 [6] Galvín P, Romero. A and Domínguez J. Fully three-dimensional analysis of high-speed train–
780 track–soil-structure dynamic interaction, Journal of Sound and Vibration 2010; 329(24): 5147-
781 5163
782 [7] Semblat JF. Modeling seismic wave propagation and amplification in 1D/2D/3D linear and
783 nonlinear unbounded media, International Journal of Geomechanics 2010; 11(6): 1-12.
784 [8] Bettess P. Infinite elements. International Journal for Numerical Methods in Engineering
785 1977; 11: 53–64.
786 [9] Houmat A. Mapped infinite p-element for two-dimensional problems of unbounded domains.
787 Computers and Geotechnics 2008; 35: 608-615.
788 [10] Enquist B and Majda A. Absorbing boundary conditions for the numerical simulation of
789 waves. Mathematics of Computation 1977; 31: 629–651.
790 [11] Liu T and Zhao C. Finite element modeling of wave propagation problems in multilayered
791 soils resting on a rigid base. Computers and Geotechnics 2010; 37: 248-257
792 [12] Kosloff D and Kosloff R. Absorbing boundaries for wave propagation problems. Journal of
793 Computational Physics 1986; 63: 363-376.

794 [13] Semblat JF, Lenti L, and Gandomzadeh A. A simple multi-directional absorbing layer
795 method to simulate elastic wave propagation in unbounded domains, International Journal for
796 Numerical Methods in Engineering 2011; 85: 1543–1563.
797 [14] Rajagopal P, Drozdz M, Skelton EA, Lowe MJS and Craster RV. On the use of the
798 absorbing layers to simulate the propagation of elastic waves in unbounded isotropic media using
799 commercially available finite element packages. NDT and E International 2012; 51: 30–40.
800 [15] Zafati E, Brun M, Djeran-Maigre I and Prunier F. Design of an efficient multi-directional
801 explicit/implicit Rayleigh absorbing layer for seismic wave propagation in unbounded domain
802 using a strong form formulation. International Journal for Numerical Methods in Engineering
803 2015; 106: 83–112.
804 [16] Li S, Brun M, Djeran-Maigre I and Kuznetsov S Hybrid asynchronous absorbing layers
805 based on Kosloff damping for seismic wave propagation in unbounded domains. Computers and
806 Geotechnics 2019; 109: 69-81.
807 [17] Bérenger JP. A Perfectly Matched Layer for the absorption of electromagnetic waves.
808 Journal of Computational Physics 1994; 114: 185-200.
809 [18] Chew WC and Weedon WH. A 3D perfectly matched medium from modified Maxwell's
810 equations with stretched coordinates. Microwave and Optical Technology Letters 1994; 7:599–
811 604.
812 [19] Chew WC and Liu QH. Perfectly matched layers for elastodynamics: a new absorbing
813 boundary condition. Journal of Computational Acoustics 1996; 4: 341–359.
814 [20] Collino F and Tsogka C. Application of the perfectly matched absorbing layer model to the
815 linear elastodynamic problem in anisotropic heterogeneous media, Geophysics 2001; 66 (1):
816 294–307.

817 [21] Wang T and Tang X. Finite-difference modeling of elastic wave propagation: a nonsplitting
818 perfectly matched approach. Geophysics 2003; 68: 1749–1755.
819 [22] Matzen R. An efficient finite element time-domain formulation for the elastic second-order
820 wave equation: A non split complex frequency shifted convolutional PML. International Journal
821 for Numerical Methods in Engineering 2011; 88: 951–973.
822 [23] Basu U and Chopra A. Perfectly matched layers for time-harmonic elastodynamics of
823 unbounded domains: theory and finite-element implementation. Computer Methods in Applied
824 Mechanics and Engineering 2003; 192: 1337-1375.
825 [24] Basu U and Chopra A. Perfectly matched layers for transient elastodynamics of unbounded
826 domains. International Journal for Numerical Methods in Engineering 2004; 59: 1039–1074.
827 [25] Basu U. Explicit finite element perfectly matched layer for transient three-dimensional
828 elastic waves. International journal for numerical methods in engineering 2009; 77:151–176.
829 [26] LS-DYNA. LS-DYNA Keyword User's Manual. Livermore Software Technology
830 Corporation 2019.
831 [27] DIANA. DIANA User's Manual, Version10.1, DIANA FEA BV 2016.
832 [28] Kucukcoban S and Kallivokas LF. Mixed perfectly-matched-layers for direct transient
833 analysis in 2d elastic heterogeneous media. Computer Methods in Applied Mechanics and
834 Engineering 2011; 200: 57–76.
835 [29] Kucukcoban S and Kallivokas LF. A symmetric hybrid formulation for transient wave
836 simulations in PML-truncated heterogeneous media. Wave Motion 2013; 50: 57–79.
837 [30] Fathi A, Poursartip B and Kallivokas LF. Time-domain hybrid formulations for wave
838 simulations in three-dimensional PML-truncated heterogeneous media. International Journal for
839 Numerical Methods in Engineering 2015; 101: 165–198.

840 [31] Brun M, Zafati E, Djeran-Maigre I and Prunier F. Hybrid asynchronous perfectly matched
841 layer for seismic wave propagation in unbounded domains, Finite Elements in Analysis and
842 Design 2016; 122: 1–15.
843 [32] Brun M, Gravouil A, Combescure A and Limam. A. Two FETI-based heterogeneous time
844 step coupling methods for Newmark and α-schemes derived from the energy method. Computer
845 methods in applied mechanics and engineering 2015; 283: 130–176.
846 [33] Gravouil A, Combescure A and Brun M. Heterogeneous asynchronous time integrators for
847 computational structural dynamics. International Journal for Numerical Methods in Engineering
848 2015; 102: 202–232.
849 [34] Grau L and Laulagnet B. Effect of horizontal wave barriers on ground vibration propagation,
850 The Journal of the Acoustical Society of America 2015; 138(3): 1334-45.
851 [35] Li S, Brun M, Djeran-Maigre I and Kuznetsov S. Explicit/implicit multi-time step co-
852 simulation in unbounded medium with Rayleigh damping and application for wave barrier.
853 European Journal of Environmental and Civil Engineering 2018.
854 [36] Belytschko T, Liu W and Moran B. Nonlinear finite elements for continua and structures.
855 Wiley, New York, 2000.
856 [37] Combescure A and Gravouil A. A numerical scheme to couple subdomains with different
857 time-steps for predominantly linear transient analysis, Computer Methods in Applied Mechanics
858 and Engineering 2002; 191:1129–1157.
859 [38] Gravouil A and Combescure A. A multi-time-step explicit–implicit method for non-linear
860 structural dynamics, International Journal for Numerical Methods in Engineering 2001; 50: 199–
861 225.
862 [39] Zuchowski L, Brun M and De Martin F. Co-simulation coupling spectral/finite elements for
863 3D soil/structure interaction problems. Comptes Rendus Mécanique 2018; 346; 408-422.

[40] Newmark NM. A method of computation for structural dynamics. Journal of the Engineering Mechanics Division (ASCE) 1959; 85: 67–94.

[41] Harari I and Albocher U. Studies of FE/PML for exterior problems of time-harmonic elastic waves. Computer Methods in Applied Mechanics and Engineering 2006; 195: 3854-3879.

[42] Lamb H. Proceedings of the 38th Royal Society of London 1903; 72: 128–130.

[43] Meza-Fajardo KC and Papageorgiou AS. A nonconvolutional, split-field, perfectly matched layer for wave propagation in isotropic and anisotropic elastic media: stability analysis. Bulletin of the Seismological Society of America 2008; 98(4):1811–1836.

[44] Festa G and Vilotte JP. The Newmark scheme as velocity-stress time-staggering: An efficient PML implementation for spectral-element simulations of elastodynamics. Geophysical Journal International 2005; 161: 789–812.

[45] Komatitsch D and Martin R. An unsplit convolutional perfectly matched layer improved at grazing incidence for the seismic wave equation. Geophysics 2007; 72: 155-167.